Predicting the metabolic capabilities of *Synechococcus elongatus* PCC 7942 adapted to different light regimes

Jared T. Broddrick[a,b], David G. Welkie[a], Denis Jallet[c,1], Susan S. Golden[a], Graham Peers[c], Bernhard O. Palsson[b,*]

[a] *Division of Biological Sciences, University of California San Diego, 9500 Gilman Dr., La Jolla, CA 92093, USA*
[b] *Department of Bioengineering, University of California San Diego, 9500 Gilman Dr., La Jolla, CA 92093, USA*
[c] *Department of Biology, Colorado State University, 251 W. Pitkin St., Fort Collins, CO 80521, USA*

A B S T R A C T

There is great interest in engineering photoautotrophic metabolism to generate bioproducts of societal importance. Despite the success in employing genome-scale modeling coupled with flux balance analysis to engineer heterotrophic metabolism, the lack of proper constraints necessary to generate biologically realistic predictions has hindered broad application of this methodology to phototrophic metabolism. Here we describe a methodology for constraining genome-scale models of photoautotrophy in the cyanobacteria *Synechococcus elongatus* PCC 7942. Experimental photophysiology parameters coupled to genome-scale flux balance analysis resulted in accurate predictions of growth rates and metabolic reaction fluxes at low and high light conditions. Additionally, by constraining photon uptake fluxes, we characterized the metabolic cost of excess excitation energy. The predicted energy fluxes were consistent with known light-adapted phenotypes in cyanobacteria. Finally, we leveraged the modeling framework to characterize existing photoautotrophic and photomixtotrophic engineering strategies for 2,3-butanediol production in *S. elongatus*. This methodology, applicable to genome-scale modeling of all phototrophic microorganisms, can facilitate the use of flux balance analysis in the engineering of light-driven metabolism.

1. Introduction

There is significant interest in engineering light-driven metabolism towards the production of fuels and chemicals. Cyanobacteria represent the simplest phototrophs and have been employed to produce a variety of products (Oliver et al., 2016). *Synechococcus elongatus* PCC 7942 (hereafter, *S. elongatus*), a genetically tractable obligate phototroph, has been engineered for the production of a wide variety of chemicals to include 3-hydroxypropinoate (Lan et al., 2015), succinate (Lan and Wei, 2016), and 1,3-propanediol (Hirokawa et al., 2016). Despite its classification as an obligate phototroph, this organism has also been engineered for mixotrophic metabolism, using carbon sources such as glycerol (Kanno and Atsumi, 2016) and glucose (Kanno et al., 2017) to generate bioproducts of interest. While experimental and computational fluxomics have been central to effective engineering of heterotrophic organisms (Adebiyi et al., 2014; King et al., 2015b), their application to the engineering of phototrophic metabolism has been limited.

Fluxomics contributes to metabolic engineering by identifying the resource partitioning through a metabolic network. Reaction fluxes are determined experimentally via ^{13}C metabolic flux analysis (MFA), or computationally using methods such as flux balance analysis (FBA) (Orth et al., 2010). Recent developments in ^{13}C MFA have resulted in characterization of photoautotrophic metabolic fluxes (Young et al., 2011) and the engineering of cyanobacteria such as *S. elongatus* (Jazmin et al., 2017). Flux balance analysis coupled with genome-scale modeling (GEM) has a long history of facilitating bioprocess design (Kim et al., 2017), and has the potential to advance the engineering of

phototrophic metabolism (Levering et al., 2015). Still, despite the availability of several phototrophic GEMs (Gudmundsson et al., 2017), there are few examples of GEMs being employed in the design of light-driven metabolic processes Carroll et al., 2018).

The potential of a GEM to engineer a metabolic network for bio-production depends on its ability to accurately predict flux through the network. Simple constraints such as the glucose and oxygen uptake rate result in accurate assessments of heterotrophic reaction fluxes (Machado and Herrgård, 2014). The ability to define the metabolic flux state with as few parameters as possible requires a mechanistic understanding of the governing constraints on the system. Recent modeling in *S. elongatus* applied photophysiology constraints, resulting in an accurate prediction of photoautotrophic growth (Broddrick et al., 2016). These photophysiology constraints, derived from a mechanistic description of photon uptake coupled with constraints on oxygen evolution, recapitulated the photoautotrophic growth curve including the transition to a light-limited linear growth curve as a result of self-shading. With the recent publication of ^{13}C MFA reaction fluxes for *S. elongatus* (Jazmin et al., 2017; Abernathy et al., 2017), it is possible to assess if the photophysiology constraints can characterize not only the photoautotrophic growth curve but also the intracellular reaction fluxes needed for model-based engineering.

GEMs can also quantify alternative electron transport (AET) within the metabolic network. Photosynthetic organisms absorb light in excess of basic biomass and maintenance requirements. A fraction of this excitation energy is dissipated upstream of the photosystem as fluorescence, heat or other non-radiative dissipation mechanisms (Schreiber et al., 1995). The remaining fraction is directed to through the photosynthetic apparatus and generates reductant and chemical energy. Excitation energy in excess of growth requirements is quenched via various AET pathways (Lea-Smith et al., 2016). AET has been shown to constitute up to 40% of the total linear electron flux through the photosystems in cyanobacteria (Helman, 2005). Characterizing and quantifying AET can facilitate engineering strategies that divert these electrons to bioproducts.

In this study we show constraining a GEM of *S. elongatus* with the photon uptake rate derived from whole-cell absorbance and the net oxygen evolution rate results in accurate predictions of metabolic fluxes. First, we generate the necessary constraints from the photophysiology of *S. elongatus* acclimated to two light intensities differing by an order of magnitude. Next, we incorporate these constraints with the GEM to predict growth rates at the two culture conditions. The resulting metabolic reaction fluxes predicted by the model showed good agreement with the experimental ^{13}C MFA results. We then use the GEM to assess alternate energy flows in *S. elongatus*, quantifying excess light energy captured by the system. Finally, we employ the modeling framework to characterize existing engineering strategies for 2,3-butanediol production in *S. elongatus*. Overall we present the governing constraints of photoautotrophic metabolism, obtained by experimentally accessible protocols, that result in accurate prediction of photoautotrophic metabolic reaction fluxes. This methodology, applicable to genome-scale modeling of all phototrophic microorganisms, can facilitate the use of flux balance analysis in the engineering of light-driven metabolism.

2. Materials and methods

2.1. Culture conditions

Synechococcus elongatus PCC 7942 wild type, stored in our laboratory's culture collection as AMC06, was cultured at 30 °C in 400 mL BG-11 medium in 1 L Roux flasks. Flasks were bubbled with air under continuous illumination with a cool fluorescent lamp in a temperature controlled incubator. Cultures were light acclimated (low light (n = 3) at 60 µmol photons $m^{-2} s^{-1}$, high light (n = 4) at 600 µmol photons $m^{-2} s^{-1}$) for 72 h, diluted and grown until mid-exponential phase

before being harvested.

2.2. Cell physiology measurements

Cell densities were manually determined using an improved Neubauer hemocytometer. Growth rates were determined based on the change in cell counts from inoculation to harvest. Cell dry weight was determined by taking 50 mL of culture (n = 3) and filtering it onto a GF/C glass microfiber filter (diameter:47 mm). Filters containing cellular biomass and media controls (n = 3) were dried at 95 °C overnight. Cellular dry weight was determined by subtracting the post-filtration mass from the pre-filtration mass, after normalizing to the media control.

2.3. Determination of cell dimensions

For imaging, thin pads of 1% (wt/vol) agarose were prepared using Mini-PROTEAN® Tetra Cell Casting Module. From this gel, 1–2 cm square pads were cut and placed onto a microscope slide and 2–5 µl cell culture liquid was added to the pad and let dry. Then a microscope slide cover was gently placed onto of the agarose pad and cells were imaged using a DeltaVision inverted epifluorescence microscope (Applied Precision, Issaquah, WA). Images were captured using a CoolSnap HD charge-coupled device (CCD) camera (Photometrics, Tucson, AZ). Cell length and width were determined using the straight line tool in ImageJ (Schindelin et al., 2015). For high light (n = 210) and low light (n = 238) acclimated cells the mean and standard deviation were determined and the mean ± 2 standard deviations was used to determine cell volume by modeling the cell shape as a core cylinder capped with two hemispheres according to the following equation:

$$Vol = \pi \left(\frac{w}{2}\right)^2 \left(l - \frac{w}{2}\right) + \frac{4}{3}\pi \left(\frac{w}{2}\right)^3$$

(1)

where l is the cell length and w is the cell width.

2.4. Pigment extraction and quantification

2.4.1. Chlorophyll a

Cells (4 mL culture) were collected by centrifugation at $10,000 \times g$ at 5 °C for 15 min. The supernatant was discarded and the cell pellet was frozen at − 80 °C until processed. Chlorophyll was extracted with 50 µL DMSO and 1950 µL of methanol, incubated in the dark for 30 min, and centrifuged at $10,000 \times g$ at 5 °C for 15 min. The pigment containing supernatant was transferred to a 1 cm path length cuvette. Absorbance spectra were collected used a Cary 60 UV–Vis Agilent spectrophotometer in scan mode (350–800 nm, scan interval of 1 nm). Chlorophyll concentrations were determined using the equations for the appropriate solvent (Ritchie, 2008).

2.4.2. Phycobilisomes

Phycobilisomes were extracted from the thawed cell pellets by resuspension in 2 mL PBS (10 mM phosphate, 150 mM NaCl, pH 7.0) with a protease inhibitor (cOmplete™, Sigma-Aldrich). Cells were lysed by sonication (Fischer Scientific Sonic Dismembrator 500, 50% power, 8 s on, 30 s off for 5 cycles) with the tube chilled in an ice bath during lysis to prevent overheating. Microscopic observation of post-sonicated samples indicated a lysis efficiency of over 90%. Lysed samples were centrifuged at $45,000 \times g$ at 5 °C for 60 min. 200 µL of the phycobilisome containing supernatant was transferred to a 96 well plate. Absorbance spectra were collected using an Infinite 200 PRO Multiplate Reader (Tecan) spectrophotometer in scan mode (400–750 nm, scan interval of 1 nm). Phycocyanobilin and apophycocyanobilin concentrations were determined using published extinction coefficients (Bennett et al., 1973) after correcting the well plate path length to a 1 cm equivalent.

2.5. Cellular absorption coefficients

Cellular absorption coefficients were determined based on published protocols (Moore et al., 1995). 1 mL of culture volume was added to 9 mL of BG-11 media and cells were collected by vacuum filtration onto a GF/C glass microfiber filter (47 mm diameter). The filter was placed on top of a 96-well plate with a plate cover along with a negative control consisting of a filter through which 10 mL of BG-11 media had passed. Absorbance spectra were collected using a Infinite 200 PRO Multiplate Reader (Tecan) in scan mode (400–750 nm). Spectra from a total of 6 wells per filter were collected, averaged, blank subtracted and normalized to an OD750 value of 0. The wavelength specific absorption coefficient was determined, along with correcting for filter amplification using the coefficients for *Synechococcus* WH103 in Moore et al. (1995), according to the following equation:

$$a_\lambda = 2.303(0.301(A_\lambda) + 0.45(A_\lambda^2)) \tag{2}$$

where A_λ is the absorbance at a given wavelength. The cell normalized absorption coefficient (a*$_{cell}$, units:cm^2 cell^{-1}) and the pigment normalized coefficient (a*$_{pigm}$, units:cm^2 µg^{-1} pigments) were determined by dividing a_λ by either the total number of cells deposited on the filter or the total pigment mass, respectively, and then multiplying the resulting value by the filter area onto which the cells were deposited (12.7 cm^2 for the 47 mm diameter GF/C filter).

2.6. Simultaneous oxygen evolution and chlorophyll fluorescence parameters

Rapid light curves (RLCs) were performed as outlined in Jallet et al. (2016). A Walz Dual PAM 100 fluorometer in a temperature controlled custom cuvette holder and a FireSting Optical Oxygen Meter were used for the simultaneous measurement of chlorophyll fluorescence and oxygen evolution. Approximately 30 mL of culture was removed and cells were pelleted by centrifugation (3000 × g, 10 min at 30 °C). Cell pellets were resuspended in fresh media to the target cell density (HL:5 × 10^8 cells mL^{-1}, LL:2.5 × 10^8 cells mL^{-1}) and kept in the dark for 10 min prior to analysis. Dark respiration rates were collected for approximately 10 min prior to running RLCs. A red actinic light (635 nm) was used to provide a saturating pulse (600 ms, 10,000 µmol photons m^{-2} s^{-1}) for fluorescence measurements. Cells were illuminated for 1 min steps at the following increasing intensities (µmol photons m^{-2} s^{-1}):

HL: 0, 8, 24, 43, 75, 109, 146, 195, 259, 339, 435, 547, 674, 844, 1033, 1565, 2386, 2924

LL: 0, 8, 24, 43, 75, 109, 146, 195, 259, 339, 435, 547, 844, 1565, 2386

The chlorophyll fluorescence parameters Fv/Fm, Y(II), qL and NPQ were determined as described (Schreiber et al., 1995; Kramer et al., 2004). Net oxygen evolution rates were normalized to cell count. Shading in the round cuvette was accounted for by calculating the attenuation across the cuvette path length according the following equation:

$$QF_{I_o} = 2 \int_{\lambda=400}^{\lambda=700} \int_{y=0}^{y=r} I_{o_\lambda}(\lambda) - I_{o_\lambda}(\lambda) e^{-a_{cell}^*(\lambda) \cdot c \cdot 2(r^2 - y^2)^{\frac{1}{2}}} dy \; d\lambda \tag{3}$$

where QF_{I_o} is the quantum flux in µmol photons m^{-2} s^{-1} at a given PAR value (I_o), λ is the wavelength, $I_{o_\lambda}(\lambda)$ is the fraction of the PAR at a given wavelength λ, r is the radius of the cuvette (0.56 cm), a_{cell}^* is the wavelength-specific absorption coefficient in cm^2 cell^{-1}, and c is the cell density in cells cm^{-3}. QF was converted to µmol photons cell^{-1} s^{-1} by multiplying QF_{I_o} by the rectangular surface area of the cuvette (width = 0.56 cm, height = 1.15 cm), converted to m^2 and dividing by the total number of cells in the cuvette. This QF value was used as the independent variable in plots of oxygen-based photosynthesis (Po) versus QF.

|	Growth rate (h^{-1})	Cell volume (µm^3)	pgDW cell^{-1}
Low Light	0.047 ± 0.004	3.4 ± 0.6	1.3 ± 0.2
High Light	0.081 ± 0.015	2.8 ± 0.3	1.0 ± 0.2

2.7. Genome-scale metabolic modeling

2.7.1. Model updates

The *S. elongatus* genome-scale model (GEM) *i*JB785 (Broddrick et al., 2016) was updated to include additional content (Table S1).

2.7.2. Simulation parameters and constraints

Simulations were performed in a similar manner to Broddrick et al. (2016). The biomass objective function was updated to account for differences in pigments between the low and high light conditions (Table 1). Demand reactions to allow dissipation of excitation energy at PSII and PSI were added to assess the minimum quantum requirement of biomass production:

DM_chla_qy2_c: chla_qy2 *_c → cholphya_c
DM_chla_qy1_c: chla_qy1 *_c → cholphya_c
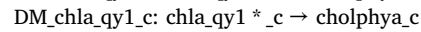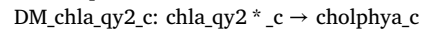
Photoautotrophic growth was simulated for a 12 h time period broken into 20 min psuedo-steady-state segments. Light was modeled coming from the side of the flask. The Roux flasks had approximately 375 mL of culture at the time of harvest which resulted in a light-facing surface area of 80 cm^2 and a path length of 4.7 cm. At the beginning of each simulation, the appropriate constraints were updated. First, the total biomass in the culture was divided by the cell dry weight to determine the total cells in the culture. Next, the photon uptake rate was determined by dividing the culture into 50 slices along the 4.7 cm path length. These slices were considered thin enough that cell shading was assumed to be negligible. Thus, we used the spectral distribution of photon flux for the given light source at the experimental irradiance ($I_0(\lambda)$), the cell specific spectral absorption coefficient (a_{cell}^*), and the cell count, to determine the photon uptake flux (I_a) in units of µmol photons (time interval)$^{-1}$ using the following equation:

$$I_a = \frac{cell}{SA} \int_{400}^{700} I_0(\lambda) a_{cell}^*(\lambda) d\lambda \tag{4}$$

where *cell* is the total number of cells in the slice and *SA* is the light-facing surface area of the slice. Light attenuated in one slice was removed from $I_0(\lambda)$ for the subsequent slices, accounting for shading along the culture path length. A running total of the absorbed light was used to set the reaction bounds of the photon exchange reactions in the GEM.

The P$_O$ vs. QF curves were fit to a Platt et al. (1980) equation for photosynthesis prediction (P$_O$), using quantum flux (QF) as the independent variable.

$$P_O = P_{max}\left(1 - e^{-\frac{\alpha \times QF}{P_{max}}}\right) e^{-\frac{\beta \times QF}{P_{max}}} \tag{5}$$

P$_{max}$ is the maximum photosynthetic rate, α and β are the parameters that describe the initial slope of the curve, and the photoinhibition (if present), respectively. These curves were used to determined the oxygen evolution rate at each slice. The total oxygen evolution across the culture path length was used to set the bounds of the oxygen exchange reaction in the GEM (reaction ID:EX_o2_e).

2.7.3. Non-growth associated maintenance

Non-growth associated maintenance (NGAM) was calculated from the experimental dark respiration rate. This value was set as the lower bound for an fictional plastoquinone oxidase (reaction ID:NGAM), which forces a minimal amount of reductant mediated oxygen consumption consistent with the observed dark respiration rate.

2.7.4. Simulation of growth

The simulation was performed by maximizing the BOF reaction using the parsimonious FBA function (pFBA) (Lewis et al., 2010) as implemented in COBRApy (Ebrahim et al., 2013). The flux through this reaction is equal to the biomass accumulation in milligrams over the 20 min time interval. This biomass was added to a running total of the total culture biomass and used to parameterize the next 20 min simulation interval. All calculations and simulations were performed using in-house scripts developed in IPython (Pérez et al., 2007).

2.8. Comparison with ^{13}C isotopically-nonstationary metabolic flux analysis

For low light simulations, the predicted pFBA flux vector from the model simulation was divided by the flux through the RPBCcx model reaction (RubisCO carboxylase) and multiplied by 100. The experimental data was normalized to 100 units of flux through the RUBP + CO2 → 3PGA + 3PGA reaction in Supplemental Table A2 for wild type *S. elongatus* PCC 7942 in Jazmin et al. (2017). For high light simulations, the same process was applied, except fluxes were normalized to the sum of the CO_2 and bicarbonate exchange fluxes (model reaction IDs:EX_co2_e, EX_hco3_e), multiplied by 100, and compared with the experimental fluxes reported in Supplemental Table 5 in Abernathy et al. (2017). Flux ranges were determined using flux variability analysis as implemented in COBRApy (Ebrahim et al., 2013) with the fraction of optimum set to 1 and the loopless option enabled.

2.9. Simulating 2,3-butanediol production

The GEM was updated with the 2,3-butanediol biosynthesis pathway as previously described (Oliver et al., 2013; Kanno et al., 2017). For model-driven production designs, non-network constraints were removed by un-constraining the reaction bounds for model reactions VPAMTr, TALA and NADTRHD as well as removing the phosphoketolase coupling constraint (Dataset S1). Photophysiology constraints were set to the upper bound of the low light acclimated culture's a^*_{cell} values and P_O vs. QF curve. Based on the culture conditions reported in Kanno et al. (2017), the total culture volume was set to 25 mL with a light-exposed cross sectional area of 70 cm^2. The glucose uptake rate was derived from Fig. 5 in Kanno et al. (2017) by taking the reported glucose consumption for each day from T = 0 to T = 3 days and dividing by the mean biomass concentration over the same time interval.

Simulations were performed as outlined in Section 2.7. To characterize the published experimental results in Kanno et al. (2017) and derive simulation parameters, the glucose uptake rate and fraction of maximum biomass production were sampled between + / − 1 standard deviation of the mean and from 0% to 30% respectively with the light level set to 30 µmol photons m^{-2} s^{-1}. Following this characterization, the glucose uptake rate was set to 0 and 0.27 mmol glucose gDW^{-1} h^{-1} for phototrophic and photoheterotrophic simulations respectively, and the fraction of maximum biomass was set to 20% for all simulations. For dark production rates the light level was set to 0 µmol photons m^{-2} s^{-1}. For the heterotrophic control, the light level was set to 0 µmol photons m^{-2} s^{-1} and the upper bound of the RubisCO carboxylase reaction (RBPCcx) was set to 0. The light intensity screen was performed by setting the inoculation density to 1 g/L and simulating 2,3-butanediol production at 0, 30, 100, 200, 300, 400, 500, 600, 700, 800 and 900 µmol photons m^{-2} s^{-1}. The inoculation density screen was performed by setting the light level to 30 µmol photons m^{-2} s^{-1} and varying the initial biomass concentration from 0.1 to 1 g/L by increments of 0.1 g/L with additional simulations at 1.5 and 2.0 g/L. The production envelope was generated by creating 450 random pairs of inoculation densities and light levels from above and simulating 2,3-butanediol production. Flux distributions were visualized using Escher (King et al., 2015a).

3. Results

In this study we set out to assess the ability of genome-scale modeling coupled with photophysiology constraints to predict metabolic capabilities in *S. elongatus*. To this end, we first collected the physiology data necessary to parameterize the models. This resulted in a comprehensive comparison of low versus high light acclimated cultures. Next, we integrated these data as constraints on the model simulations, comparing model simulations with in vivo growth rates and fluxes. We then assessed the alternate energy flows through the photosystems as a result of the absorption of excess excitation energy. Finally we employed the photophysiology constraints to characterize and engineering 2,3-butanediol production strategies in *S. elongatus*.

3.1. Photoacclimation of S. elongatus PCC 7942

3.1.1. Cell physiology at low and high light acclimation

S. elongatus was acclimated and cultured at a high light condition of 600 µmol photons m^{-2} s^{-1} (HL, n = 4) and a low light condition of 60 µmol photons m^{-2} s^{-1} (LL, n = 3). Specific growth rates were 0.081 ± 0.015 and 0.047 ± 0.004 h^{-1} respectively for HL and LL cultures. While cells grown at both light levels had approximately the same cell width (1.2 ± 0.1 and 1.1 ± 0.1 µm at HL and LL respectively), LL cells were significantly longer resulting in a 20% increase in cell volume at LL (Table 1).

3.1.2. Cellular pigmentation at low and high light acclimation

There were significant differences in light harvesting pigments as a result of photoacclimation. Total pigments (phycocyanin (PC), allophycocyanin (APC) and chlorophyll *a* (chla)) at LL were 4.9 fold higher than at HL (Table 2). Chla and APC increased at a similar rate (3.4 and 3.8 fold respectively). Almost all chla in *S. elongatus* is contained within the photosystems (Stamatakis et al., 2014) and APC is a linker pigment-protein complex physically and energetically connecting the light harvesting PC with the photosystems. Thus, this increase in chla and APC is likely attributed to an increase in the number of PSI and PSII complexes present at LL. The light harvesting pigment-protein complex PC increased 5.7 fold at LL compared to HL. The larger -fold increase in PC versus APC suggests not only did the number of phycobilisomes increase but the rod length of each phycobilisome increased at LL compared to HL. The phycobilisomes constituted 28% of the cellular biomass at LL compared to 7% at HL.

The pigment content and composition of the cell dictates its light harvesting capacity. This cell-specific absorption coefficient is an important modeling parameter as it determines the photon uptake rate

Table 2
Comparison of pigments in *S. elongatus* acclimated to low and high light.

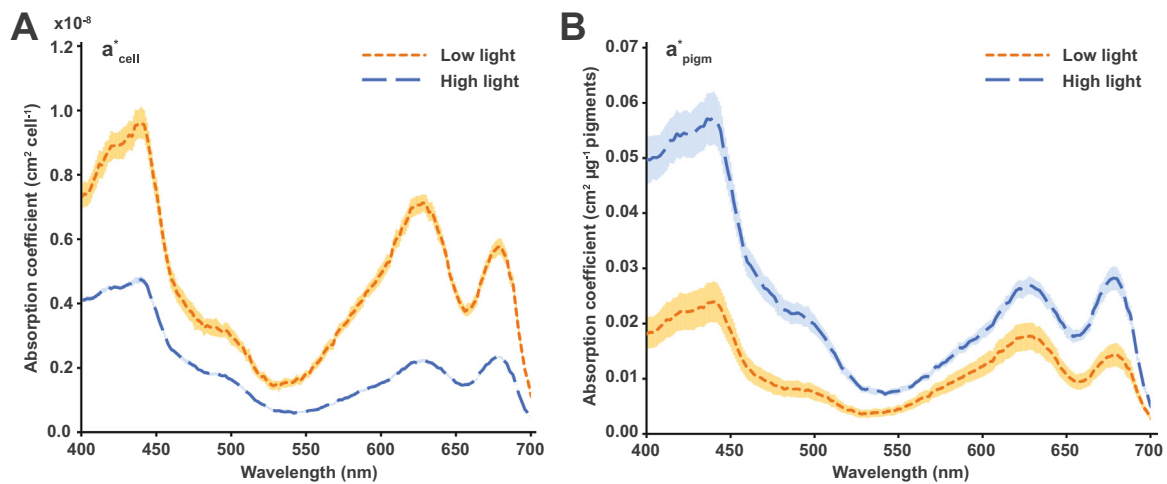| | Chl *a* (pg/cell) | PC (pg/cell) | APC (pg/cell) | PC: Chl *a* | APC: Chl *a* | PC: APC | Ratios (LL: HL) | | | |
							Total pigments	Chl *a*	PC	APC
Low light	0.037 ± 0.002	0.29 ± 0.05	0.08 ± 0.02	7.8	2.2	3.6	4.9	3.4	5.7	3.8
High light	0.011 ± 0.000	0.05 ± 0.01	0.02 ± 0.00	4.6	1.9	2.4				

Fig. 1. Cell- and pigment-specific absorption coefficients for *S. elongatus* acclimated to low and high light. (A) Cell-specific absorption coefficient. (B) Pigment-specific absorption coefficient. The pigment mass includes phycocyanin, allophycocyanin and chlorophyll *a*. Shaded areas represent one standard deviation from the mean (HL n = 4, LL n = 3).

and the extent of self-shading that occurs in the culture. We compared the cell normalized absorption coefficient (a^*_{cell}) and the pigment normalized coefficient (a^*_{pigm}) at both light levels (Fig. 1). LL acclimation resulted in 2.3 times more light absorbed per cell than the HL cells, despite the 4.9 fold increase in total pigments. This decrease in light capture efficiency on a per-pigment basis is illustrated in the LL to HL a^*_{pigm} ratio of approximately 0.5 (Fig. 1B, area under the curve:HL:7.4 vs LL:3.6 cm^2 µg^{-1} nm^{-1}). Thus, while low light acclimation allowed *S. elongatus* to absorb more light per cell, there were diminishing returns with respect to the resources needed to harvest the light energy.

3.2. Photophysiology of S. elongatus at low and high light

3.2.1. Photon uptake constraint

As the GEM requires quantitative incorporation of photophysiology constraints, we converted both the photon uptake and the photosynthesis versus irradiance (P vs. I) curve into a model-compatible format. The photon uptake rate is derived from the photosynthetically available radiation (PAR) spectrum and the a^*_{cell} values. The PAR spectrum is a wavelength density function describing the relative distribution of photons across the visible-light region of the electromagnetic spectrum. For example, a red LED exclusively delivers photons in the 600–700 nm range while a white LED distributes the photons over a broader range of wavelengths. While the PAR spectrum describes the wavelength-specific delivery of light, the a^*_{cell} describes the wavelength-specific attenuation of light. For example, the cyanobacterial light harvesting pigment phycocyanin preferentially captures orange and red photons and is responsible for the absorption maximum at 620 nm in Fig. 1. Therefore, the intersection of the PAR spectrum and the a^*_{cell} quantifies the photon uptake rate.

3.2.2. Oxygen evolution constraint

We simultaneously measured chlorophyll fluorescence parameters and oxygen evolution using a rapid light curve (RLC) protocol (Jallet et al., 2016). In an improvement over previous photoautotrophic modeling of *S. elongatus* (Broddrick et al., 2016), we converted the incident light (PAR) to the quanta of light absorbed by the cells (quantum flux, QF). This representation is necessary to convert between light sources of different spectral quality. In the previous modeling study (Broddrick et al., 2016), the P vs. I curve was determined with a white LED and the culture light source was a fluorescent lamp. For *S. elongatus*, these light sources result in similar QF rates. In this study, the oxygen evolution and fluorescence were collected using a red actinic

light, while the cells were cultured under fluorescent light. These light sources have dramatically different spectral qualities; thus, necessitating a conversion.

Upon conversion the P vs. I curve becomes a P vs. QF curve and describes the maximum photosynthesis rate as a function of photon uptake. In this study we used oxygen evolution as a proxy for photosynthesis (P_O). While a culture under full diurnal, solar irradiance may experience a wide variety of QF values, constant light cultures only experience a small section of the P_O vs. QF curve. Thus, the only relevant section of the curve is the maximum QF (QF_{max}), representative of photon capture rates of cells closest to the light source, and the minimum QF (QF_{min}), representative of the photon capture rate at the point farthest from the light source, attenuated by cell shading. Thus, we report both the maximum QF (QF_{max}) and the mean QF (QF_{mean}), representative of the average photon capture rate across the full path length.

To induce sufficient fluorescence signal, PAM measurements often require high cell densities. The resulting increase in cell shading decreases the quanta of light absorbed across the path length of the sample cuvette. In an improvement over the previous modeling effort (Broddrick et al., 2016), we calculated the photon uptake accounting for cuvette shape, path length, cell density and cellular pigmentation (Wagner et al., 2006). This transformation dramatically affected the calculated oxygen evolution rate at a given photon absorption rate (P_O vs. QF) (Fig. S1).

3.2.3. Growth rate is correlated to mean oxygen evolution rate

P_O versus QF curves showed the LL acclimated cells had a significantly steeper light limited slope of photosynthesis, α, and a higher maximum photosynthetic rate, P_{max}, compared to HL cultures (Fig. 2A). This resulted in similar cell-specific maximum oxygen evolution rates at the experimental QF for the two light levels with the HL P_O at QF_{max} approximately 20% higher than the LL condition (Table 3, $P_{O_{max}}$). Comparing the oxygen evolution rates at the respective QF_{mean} value for both acclimation conditions, this difference increased to 37% (Table 3, $P_{O_{mean}}$), quantifying the negative impact of cell shading on culture productivity. When the P_O versus QF curves were normalized to gram dry cell weight, the difference in mean oxygen evolution rate increased to 75% (Fig. 2B), which is similar to the difference in specific growth rate (72%, Table 1).

3.2.4. Chlorophyll fluorescence parameters

Interpretation of chlorophyll fluorescence measurements in cyanobacteria differs from that in algae and higher plants (Schuurmans et al.,
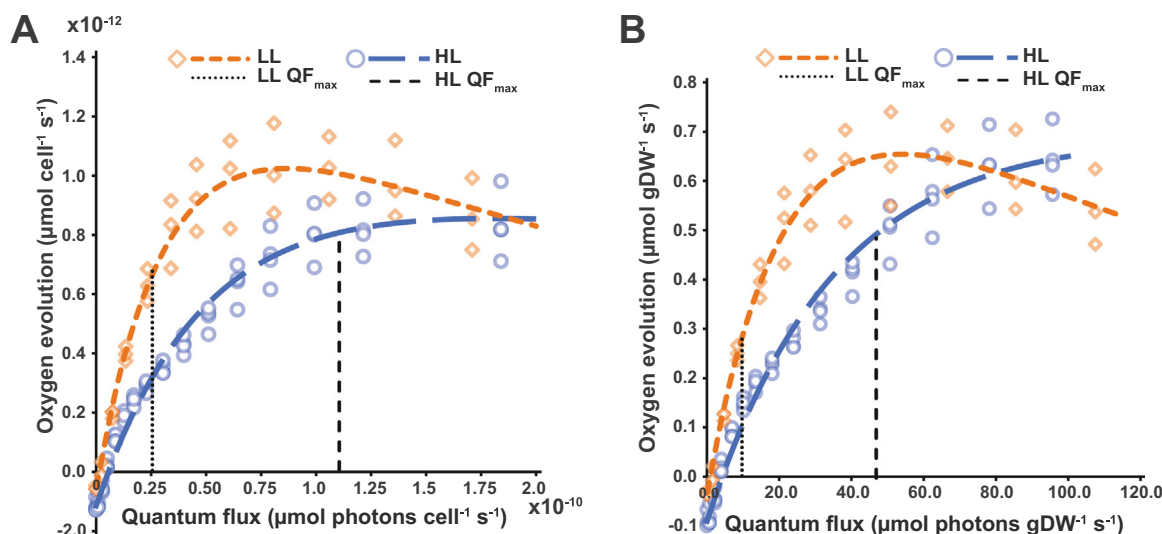
Fig. 2. Oxygen evolution versus quantum flux for *S. elongatus* acclimated to low and high light. (A) Cell-specific P_o versus QF curves. (B) Dry cell weight-specific P_o versus QF curves. Vertical dashed lines represent the maximum quantum flux received by the cultures at the experimental irradiance. Abbreviations. LL: low light, HL: high light, QF: quantum flux.

2015; Ogawa et al., 2017). As such, we report the maximum quantum yield of PSII (Fv/Fm), the effective quantum yield of PSII as a function of QF (Y(II)), and the fraction of open reaction centers (qL) (Table 3 and Fig. S2). However, the values were not quantitatively integrated with our model simulations. *S. elongatus* PCC 7942 lacks the orange carotenoid protein that confers the blue light activated phycobilisome fluorescence quenching mechanism in cyanobacteria (Kirilovsky and Kerfeld, 2012) and we did not observe non-photochemical quenching (NPQ) induced fluorescence in either acclimation condition. The effective quantum yield was approximately two-fold higher for the LL acclimated cells (0.33 ± 0.01 vs. 0.15 ± 0.01 at LL and HL respectively), suggesting an increase in excitation energy diverted to PSI, consistent with previous observations in cyanobacteria (Ogawa et al., 2017).

3.3. Genome-scale modeling of *S. elongatus* at low and high light

3.3.1. Simulating photoautotrophy

The photophysiology results were translated into modeling constraints to simulate photoautotrophic growth of *S. elongatus*. The a*$_{cell}$ coupled with the experimental PAR intensity and spectral quality of the fluorescent light was used to determine the photon uptake constraint for the simulations. This uptake value, equivalent to QF, was used to determine the oxygen evolution rate of the culture. This value constrained the oxygen exchange flux for the simulations. The biomass objective function (BOF) (Feist and Palsson, 2010) defines which metabolites and in what ratio must be synthesized to generate the macromolecular cellular components necessary for growth. We updated the BOF to reflect the differences in pigment mass between the two growth conditions prior to performing simulations.

The quality of the model simulations depends on the accuracy of the experimental photophysiology parameters. Thus, we not only simulated

growth using the mean values, but also the upper bound (UB) and lower bounds (LB) of the P_O vs. QF curves, a*$_{cell}$ and dry cell weight (pg cell^{-1}). As the experimental growth curves are based on cell counts, the dry cell weight converts the biomass accumulation predicted by the model to cell counts; thus, having an impact on the accuracy of the model growth rate predictions.

The model predicted a LL mean growth rate of $0.033\,\text{h}^{-1}$(UB:0.044, LB:0.025) compared to an experimental value of $0.047 \pm 0.004\,\text{h}^{-1}$ representing a 30% underestimation by the model (Fig. 3). For the HL condition the model predicted a mean growth rate of $0.051\,\text{h}^{-1}$ (UB:0.067, LB:0.039) compared to an experimental value of $0.081 \pm 0.015\,\text{h}^{-1}$ representing a 38% underestimation by the model (Fig. 3). While the upper bound of the simulations values approached the range of the experimental observations, the model tended to underestimate the growth rate at both high and low light.

3.3.2. Maintenance energies at low and high light acclimation

We explored whether or not maintenance energy requirements forced upon the model could explain the growth rate discrepancies. Maintenance energies in phototrophs differ from that of heterotrophs as the energy source, light, is uncoupled from the carbon source, inorganic carbon. Thus, as long as the culture is not light-limited, maintenance energy costs will not affect growth rate.

Growth-associated maintenance (GAM), represented as growth-dependent ATP consumption, has been inconsistently applied to phototrophic GEMs. Genome-scale models of the cyanobacterium *Synechocystis* sp. PCC 6803 include GAM values ranging from 53 to $1.3\,\text{mmol ATP gDW}^{-1}\,\text{h}^{-1}$ (Nogales et al., 2012; Knoop et al., 2013). GAM requirements in our *S. elongatus* GEM include a growth associated maintenance cost of $30\,\text{mmol ATP gDW}^{-1}\,\text{h}^{-1}$; however, this is a largely arbitrary value. Our GEM sets the non-growth associated

Table 3
Comparison of photosynthetic rates in *S. elongatus* acclimated to low and high light. The chlorophyll fluorescence parameter qL is reported for QF_{mean}.

| | QF_{max} [a] | QF_{mean} [a] | $P_{o max}$ [b] | $P_{o mean}$ [b] | Fv/Fm | qL | Ratios (HL: LL) | |
							$P_{o max}$	$P_{o mean}$
Low Light	2.5×10^{-11}	1.6×10^{-11}	$6.6 \pm 0.8 \times 10^{-13}$	$4.6 \pm 0.5 \times 10^{-13}$	0.30	0.93	1.2	1.4
High Light	1.1×10^{-10}	6.0×10^{-11}	$8.1 \pm 0.7 \times 10^{-13}$	$6.3 \pm 0.4 \times 10^{-13}$	0.20	0.71		

[a] μmol photons cell^{-1} s^{-1}.
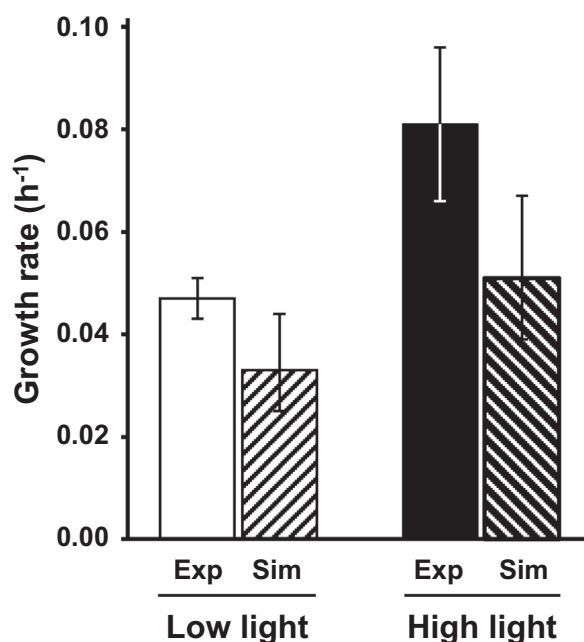[b] μmol O_2 cell^{-1} s^{-1}.

Fig. 3. Experimental versus simulated growth rates for *S. elongatus* acclimated to low and high light. For experimental values, error bars represent the standard deviation (HL: n = 4, LL: n = 3). For the simulation values, the error bars represent the model upper and lower bounds of the model predictions based on the error of the experimental inputs. Abbreviations. Exp: experimental, Sim: simulated.

maintenance (NGAM) to the dark respiration rate. This value represents the residual reductant-mediated oxygen consumption that is necessary to maintain viability in the absence of light; with 1 mmol O_2 corresponding to 4 mmol electrons being consumed. This value varies with the incident irradiance. We observed dark respiration rates of 0.41 and 0.15 mmol O_2 gDW^{-1} h^{-1} for *S. elongatus* at HL and LL respectively. Finally, there is an NGAM cost associated with the repair of the photosystem II (PSII) D1 subunit. This subunit is damaged at a rate proportional to PSII flux (Allakhverdiev and Murata, 2004), is independent of growth rate, and incurs an ATP and GTP cost at the ribosome to biosynthesize a replacement subunit.

Upon removing all GAM and NGAM requirements, the growth rate was unchanged at LL and HL. Additionally, using the mean cellular and photophysiology parameters, we quantified the energy in excess of growth and maintenance requirements by fixing the growth rate at the maximum value and optimizing for either an ATP hydrolysis reaction or a plastoquinone-mediated oxygen consumption reaction. At LL, an ATP hydrolysis flux of 19 mmol ATP gDW^{-1} h^{-1} and a respiratory flux of 0.7 mmol electrons gDW^{-1} h^{-1} could be sustained above and beyond growth and maintenance requirements. At HL, these values increased to 122 mmol ATP and 2.0 mmol electrons gDW^{-1} h^{-1}, suggesting the cultures are not light limited at either irradiance. Thus, the growth rate discrepancy between our simulations and the observed experimental values was not due to excessive maintenance energy requirements forced on the model.

The result suggesting the LL acclimated cells had excess energy ran contrary to the lower observed growth rate. Using the reductant excess of 0.7 mmol electrons gDW^{-1} h^{-1}, we back-calculated the overestimation of photon uptake. This analysis suggested a photon flux overestimation of less than 3% could account for the observed excess reductant. The photon uptake is parameterized by the a*$_{cell}$ parameter and this 3% overestimation falls within 1 standard deviation of the LL a*$_{cell}$ (5.3%). Thus, while the mean photon uptake rate determined for the LL condition represents an overestimation, the true value likely lies within 1 standard deviation of the determined mean.

3.4. Comparison of GEM predicted reaction fluxes with ^{13}C MFA

3.4.1. Parsimonious FBA fluxes were consistent with ^{13}C MFA values

While growth rate can be inferred from empirical models, genome-scale models have the advantage of predicting the flux for all biochemical reactions in the metabolic network. In the case of *S. elongatus*, constraining the oxygen evolution rate with net P_O, the photon uptake rate with QF and the biomass objective function with the light-condition-specific cellular composition, reaction fluxes are predicted for 861 intracellular reactions. Recent studies have used ^{13}C metabolic flux analysis (MFA) to experimentally determine the reaction flux for central metabolism in *S. elongatus* (Jazmin et al., 2017; Abernathy et al., 2017). We compared our LL condition predicted reaction fluxes with those published for *S. elongatus* at a similar growth rate (Jazmin et al., 2017), normalized to 100 units of RubisCO carboxylase flux to account for the slight difference in growth rate. The predicted reaction fluxes, determined using parsimonious FBA (pFBA) (Lewis et al., 2010), showed remarkable similarity to the experimental values (coefficient of determination = 0.99, Figs. 4 and 5A, B). The primary difference was in metabolic fluxes surrounding the malate dehydrogenase (MDH); a reaction that was inferred from the ^{13}C MFA data, but to date the gene responsible for catalyzing this reaction is unidentified in *S. elongatus* PCC 7942.

We compared our HL predicted reaction fluxes with those published for *S. elongatus* PCC 7942 at near optimal growth rates (Abernathy et al., 2017). Again, pFBA flux predictions showed good agreement with the experimental values (coefficient of determination =;0.98, Figs. 6 and 5C, D). The primary discrepancies were in the phosphatase reactions in the Calvin-Benson cycle. However, the net flux into and out of these reactions were in agreement. Overall, the GEM flux predictions constrained by photophysiology constraints were consistent with ^{13}C MFA results across the range of observed growth rates.

3.4.2. Flux variability analysis of the optimal solution space

Solutions to genome-scale models often have multiple, mathematically equivalent flux states at the optimal growth rate. The pFBA solution described in Section 3.4.1 is only one of potentially multiple equivalent solutions. Using flux variability analysis (FVA), we explored whether or not alternate optimal solutions existed for the LL and HL models as these alternate solutions may resolve discrepancies between the pFBA predicted flux solution and the ^{13}C MFA determined values. For both LL and HL conditions, FVA ranges were narrow for all reactions for which ^{13}C MFA data exists, except those connected to an ATP or reductant consuming reaction (Fig. 5a,c). As discussed in Section 3.3.2, both conditions have ATP and reductant pools in excess of growth and maintenance requirements. As a result, the FVA ranges for these reactions are wide as the available energy pools can drive flux through these energy consuming reactions. Therefore, the minor discrepancies in flux predictions are likely a result of the minimization of total flux performed by pFBA.

3.5. Predicted excitation energy routes in S. elongatus

The GEM's biomass objective function defines the energetic requirements for growth down to the metabolite level. Comparing constrained versus unconstrained photon uptake enabled an assessment of excitation energy absorbed in excess of biosynthesis and maintenance needs. We simulated growth using the upper bound constraints as they more closely recapitulated in vivo growth rates and thus, realistic energy needs.

At low light, with a QF of 2.0×10^{-11} µmol photon $cell^{-1}$ s^{-1}, the model where all excess excitation energy can be dissipated upstream of the photosystems (unconstrained) predicted only 33% of the excitation energy was necessary to satisfy the electron needs for biomass production and maintenance. We then constrained the photon uptake to account for the entire quanta of absorbed photons. The GEM includes
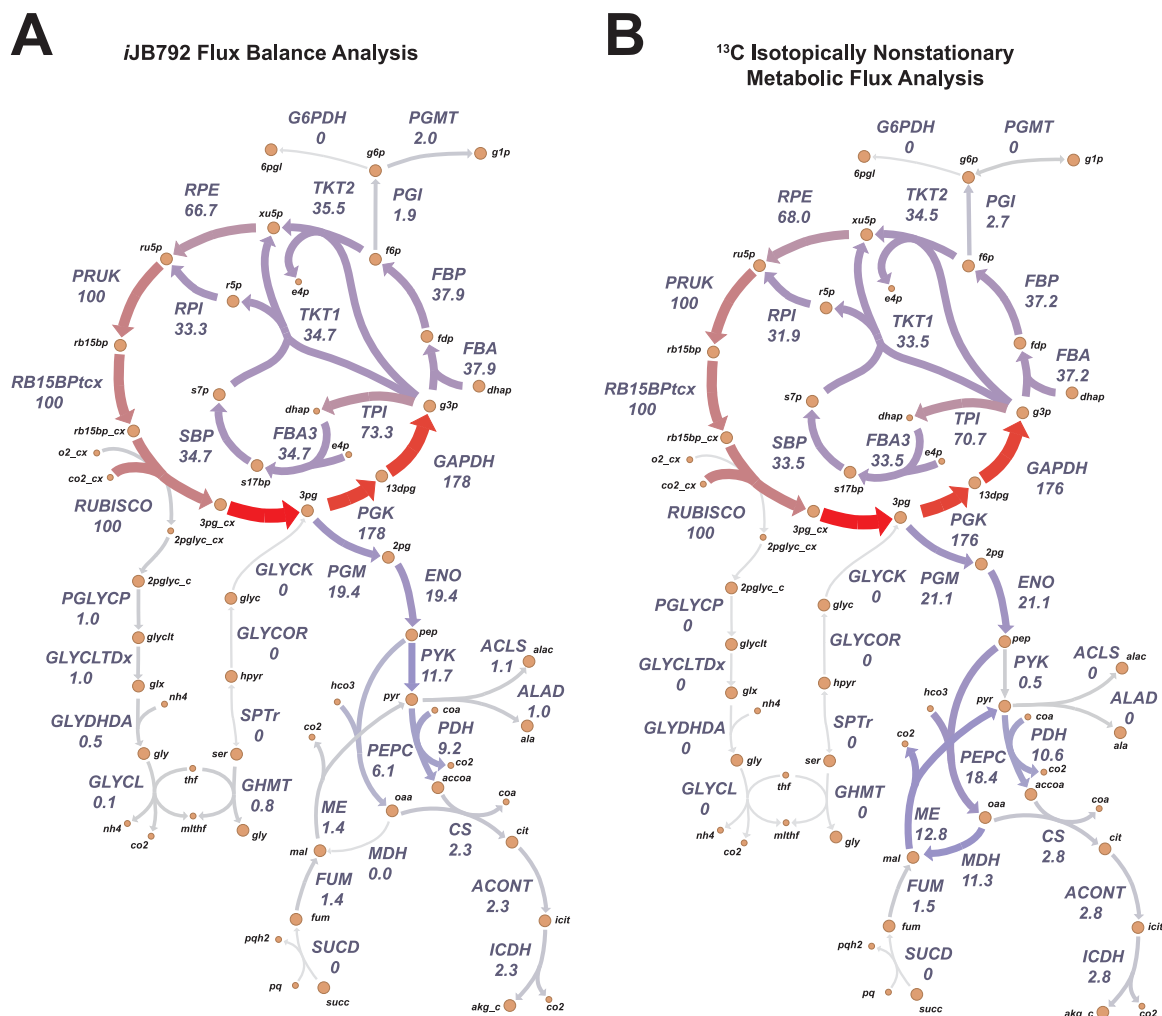
Fig. 4. Simulated versus experimental metabolic reaction fluxes for *S. elongatus* at low growth rates. (A) Predicted fluxes at low light by the *S. elongatus* genome-scale model *i*JB792. (B) Experimental reaction fluxes for *S. elongatus* as reported in Jazmin et al. (2017). Metabolic reactions and metabolites are indicated by their BiGG identifier (bigg.ucsd.edu). Flux values normalized to 100 units of RubisCO carboxylase flux are shown below the reaction abbreviations.

experimentally determined wavelength-specific energy transfer efficiencies (Stamatakis et al., 2014). Based on these values and the emission spectra of the growth light, approximately 30% of the QF is lost before reaching the reaction centers. This quanta, along with the biomass and maintenance requirements accounted for 63% of the absorbed photons. The remaining 37% was consumed by alternative electron transport (AET). At high light, with a QF of 7.5×10^{-11} µmol photon cell^{-1} s^{-1}, the unconstrained model predicted only 11% of the excitation energy was necessary to satisfy the electron needs for biomass production and maintenance. After accounting for wavelength-specific energy transfer efficiencies, 58% of the absorbed QF was consumed by AET.

The AET predicted by the model depends on their relative metabolic cost. The simulations predicted relatively high flux through PSI, even at low light. The model includes a basal PSI superoxide generation rate of 1% (Tichy et al., 1999), while PSII includes a D1 repair cost proportional to flux. The model flux predictions preferentially routed excitation energy through PSI since the combined action of superoxide dismutase and catalase detoxifies the ROS to water with no energy input required. Compared to the unconstrained simulation, the constrained simulation predicted an increase in charge recombination at PSII which increases damage to the PSII D1 protein. This damage is mitigated by *de novo* synthesis of a new protein at a significant ATP/GTP cost at the ribosome. The model predicted increased cyclic electron flow around PSI is required to generate the chemical energy necessary for D1 protein

biosynthesis (Table 4). Thus, the D1 repair cost determines both the predicted bifurcation of excitation energy between PSII and PSI and the cyclic electron flow rate, balancing ATP and reductant ratios necessary to satisfy photodamage mitigation and repair mechanisms. A summary of predicted excitation energy routing, D1 repair costs and quantum yields of carbon fixation and oxygen evolution are shown in Table 4.

3.6. Model-driven engineering of 2,3-butanediol production in S. elongatus

3.6.1. A phosphoketolase-based engineering strategy for 2,3-butanediol production

The chemical precursor (R,R)-2,3-butanediol (23BD) has been successfully produced in *S. elongatus* via both phototrophic (Oliver et al., 2013) and photomixotrophic strategies (McEwen et al., 2012; Kanno et al., 2017). We explored the ability of the photophysiology constrained GEM to optimize 23BD production in *S. elongatus*. We added the 23BD biosynthesis pathway to the GEM (Dataset S1) and removed the non-network constraints. These constraints are restrictions on pathway usage and magnitude that were necessary to recapitulate published in vivo gene essentiality data (Rubin et al., 2015; Broddrick et al., 2016); however, the organism can be engineered to overcome these constraints. The model suggested an optimal solution that uses the phosphoketolase (PKT) pathway to bypass lower glycolysis (Fig. 7b). PKT uses the Calvin-Benson-Bassham (CBB) cycle intermediates fructose-6-phosphate (F6P) or xylulose-5-phosphate as substrates. Previous
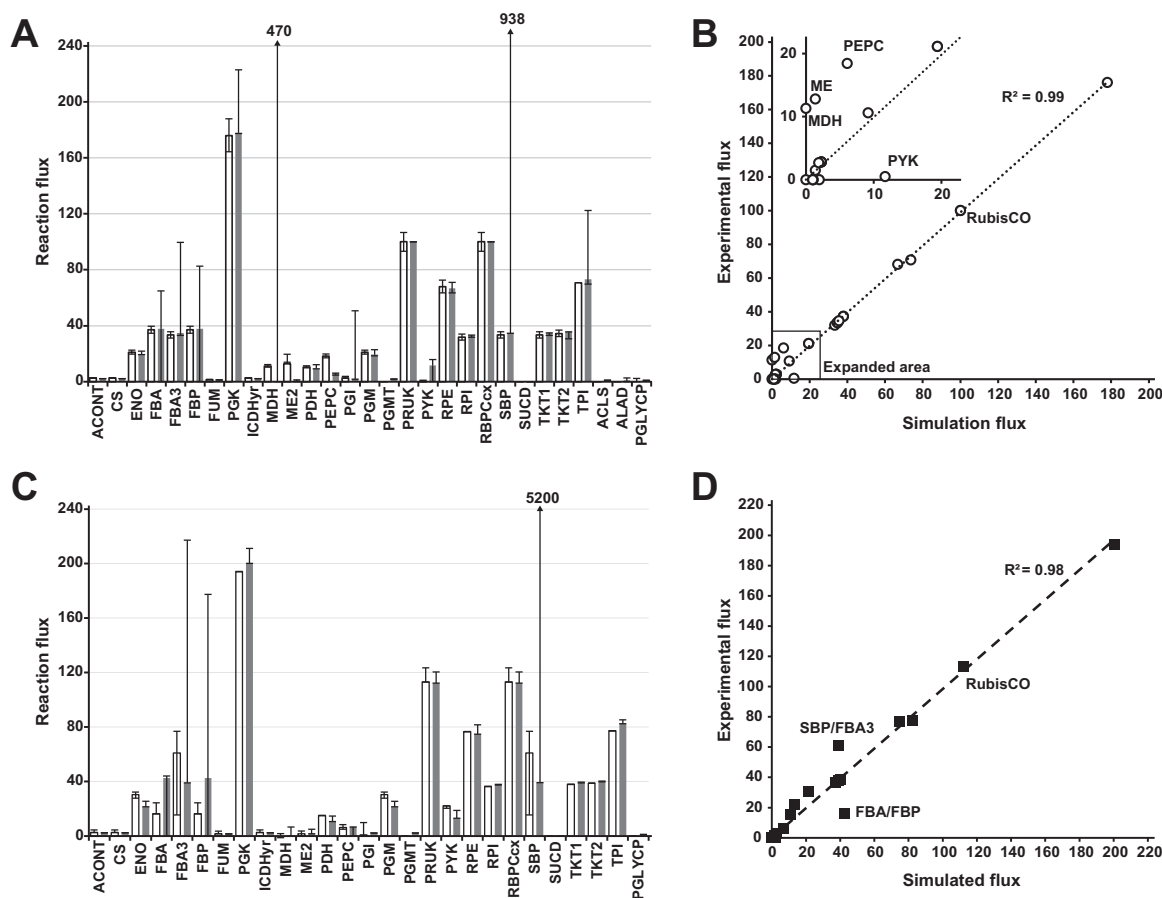
Fig. 5. Correlation between simulated and experimental metabolic reaction fluxes for *S. elongatus*. (A) Comparison of low light predicted fluxes (gray bars) and experimental fluxes (white bars) reported in Jazmin et al. (2017). Flux ranges determined by flux variability analysis are shown for the predicted fluxes. Upper bounds that exceed the Y-axis scale are indicated by an arrow and the upper bound flux value. (B) Correlation between low light predicted fluxes and experimental fluxes reported in Jazmin et al. (2017). (C) Comparison of high light predicted fluxes (gray bars) and experimental fluxes (white bars) reported in Abernathy et al. (2017). Flux ranges determined by flux variability analysis are shown for the predicted fluxes. Upper bounds that exceed the Y-axis scale are indicated by an arrow and the upper bound flux value. (D) Correlation between high light predicted fluxes and experimental fluxes reported in Abernathy et al. (2017). Metabolic reactions and metabolites are indicated by their BiGG identifier (bigg.ucsd.edu). For (A) and (B), flux values are normalized to 100 units of RubisCO carboxylase flux. For (C) and (D) flux values are normalized to 100 units of inorganic carbon uptake. Abbreviations: ACONT: aconitase, CS: citrate synthase, ENO: enolase, FBA: fructose-bisphosphate aldolase, FBA3:sedoheptulose 1,7-bisphosphate D-glyceraldehyde-3-phosphate-lyase, FBP:fructose-bisphosphatase, FUM: fumarase, PGK:phosphoglycerate kinase, ICDH:isocitrate dehydrogenase, MDH: malate dehydrogenase, ME: malic enzyme, PDH: pyruvate dehydrogenase, PEPC:phosphoenolpyruvate carboxylase, PGI:glucose-6-phosphate isomerase, PGM:phosphoglycerate mutase, PGMT: phosphoglucomutase, PRUK: phosphoribulokinase, PYK:pyruvate kinase, RPE:ribulose-5-phosphate 3-epimerase, RPI: ribose-5-phosphate isomerase, SBP: sedoheptulose-bisphosphatase, SUCD: succinate dehydrogenase, TKT1: transketolase (S7P → R5P + X5P), TKT2:Transketolase (F6P → E4P + X5P), TPI: triosephosphate isomerase, ACLS: acetolactate synthase, ALAD:L-alanine-dehydrogenase, PGLYCP: phosphoglycolate phosphatase.

modeling in *S. elongatus* also suggested this pathway was optimal; however, since the enzymes that participate in lower glycolysis were determined to be essential in vivo (Rubin et al., 2015), it was concluded this bypass was not active during photoautotrophic conditions (Broddrick et al., 2016). However, a heterologous PKT pathway has been successfully engineered into *S. elongatus* for the production of acetone directly from CO_2 (Chwa et al., 2016), suggesting this pathway can be engineered to carry flux under photoautotrophic conditions. Additionally, *S. elongatus* engineered to consume exogenous glucose was shown to have an elevated F6P pool (Kanno et al., 2017), one of the PKT substrates. Thus, hypothesizing an overexpressed PKT pathway could tap into this F6P pool, we performed an *in silico* comparison of the PKT pathway to the published oxidative pentose phosphate (OPP) engineered pathway (Kanno et al., 2017) for converting exogenous glucose into 23BD (Fig. 7a,b).

3.6.2. Model-driven characterization of photomixotrophic 23BD production

First, using the model as a framework, we characterized the OPP engineered pathway results to derive the necessary parameters for

comparison. Based on the published culture conditions, the feedstock was likely low light acclimated (30 µmol photon m^{-2} s^{-1}); thus, we used the photophysiology values (a*$_{cell}$, P$_O$ vs. QF, pigment composition, etc.) from our LL acclimated culture as simulation parameters. Using the published results from Kanno et al. (2017), we determined the glucose uptake rate of the optimized strain was approximately 0.25 ± 0.08 mmol glucose gDW^{-1} h^{-1} during the first 3 days of culturing. Using a value of 0.27 mmol glucose gDW^{-1} h^{-1} and the biomass production rate set to 20% of the maximum, the experimental results were accurately recapitulated (Fig. S3a-c). Thus, these values were used for simulating photomixotrophic production of 23BD.

Using the derived glucose uptake and biomass partitioning values, we compared flux simulations from the OPP engineered pathway and the PKT designed pathway. Both designs resulted in identical titers and specific productivities at the published experimental conditions in Kanno et. al. (30 µmol photon m^{-2} s^{-1}, 1 g/L inoculation density) and were consistent with the experimental results (Fig. 8a). Parsimonious FBA flux predictions between the OPP and PKT designs suggested that while both designs resulted in the same 23BD titer, the PKT design
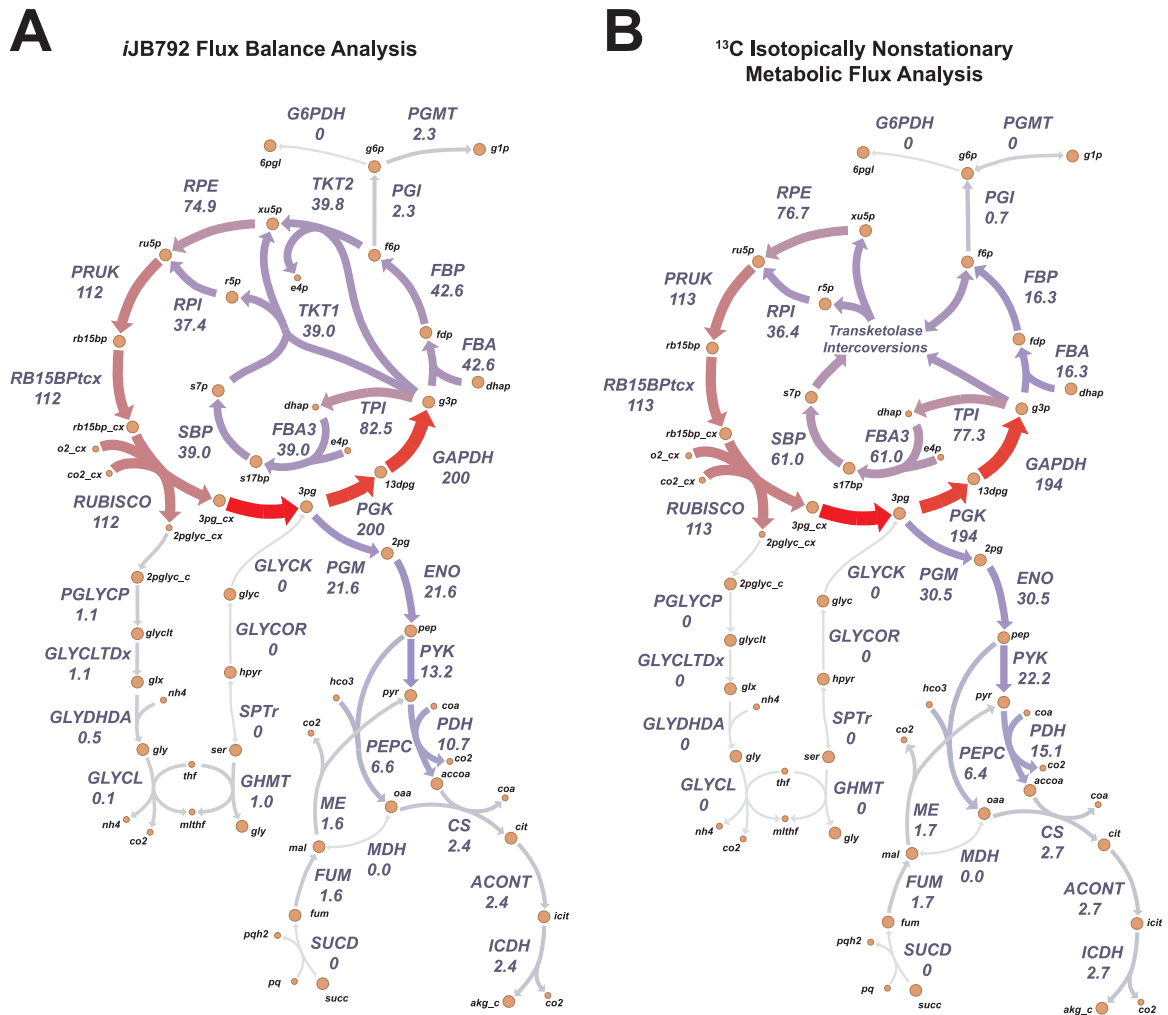
Fig. 6. Simulated versus experimental metabolic reaction fluxes for *S. elongatus* at high growth rates. (A) Predicted fluxes at high light by the *S. elongatus* genome-scale model *i*JB792 at low light. (B) Experimental reaction fluxes for *S. elongatus* as reported in Abernathy et al. (2017). Metabolic reactions and metabolites are indicated by their BiGG identifier (bigg.ucsd.edu). Flux values normalized to 100 units of inorganic carbon uptake are shown below the reaction abbreviations.

Table 4
Predicted excitation energy flow in *S. elongatus* acclimated to low and high light. Φ_{CO_2}: quantum yield of net carbon fixation, Φ_{O_2}: quantum yield of net oxygen evolution. Abbreviations: ET: energy transfer, PSII: photosystem II, PSI: photosystem I, CEF: cyclic electron flow, CR: charge recombination.

	Fraction of absorbed quanta									State Transition	
	ET loss	PSII	PSI	CEF	PSII CR	PSI/PSII	D1 repair cost[1]	Φ_{CO_2}[2]	Φ_{O_2}[2]	PSI:PSII[3]	Y(II)[4]
High light	0.31	0.09	0.60	0.54	0.04	6.7	3.2×10^{-10}	0.009	0.010	2.1	2.1
Low light	0.29	0.17	0.54	0.36	0.03	3.2	0.6×10^{-10}	0.028	0.031		

[1] μmol ATP cell^{-1} s^{-1}.

[2] μmol x μmol^{-1} photon.

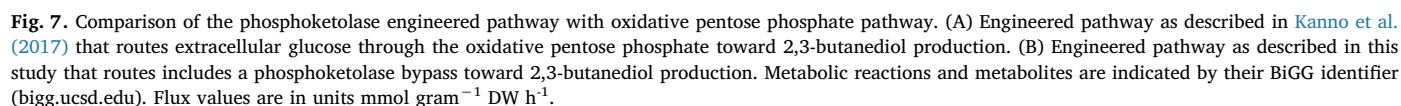[3] (High light PSI/PSII) x (Low light PSI/PSII)$^{-1}$.

[4] (Low light Y(II)) $\times$ (High light Y(II))$^{-1}$.

required 40% less flux through the CBB cycle (Fig. 7a,b). Additionally, the PKT design avoids carbon loss as CO_2 at both the OPP reaction phosphogluconate dehydrogenase and at the pyruvate dehydrogenase (PDH) reaction. The OPP pathway does generate 2 equivalents of NADPH per glucose; however, these reactions would have to compete with photosynthesis for the oxidized NADP+ pool, which may limit the flux through the OPP pathway. The phosphoketolase enzyme cleaves F6P into acetyl phosphate, which is converted to acetyl-CoA and used to generate biomass, and erythrose 4-phosphate, a CBB intermediate. Thus, the PKT pathway coupled with a PDH knockout would result in a maximum biomass partitioning of 33% (2 out of 6 carbons from

glucose) and effectively uncouple the CBB from biomass production and towards 23BD biosynthesis. The flux distributions suggest the PKT design could provide advantages over the OPP pathway, especially at high irradiances when the redox state of the NADPH pool may inhibit OPP flux.

3.6.3. Simulation of phototrophic and photomixotrophic 23BD production

Next, we assessed the impact of cell shading on 23BD production. Using an inoculation density of 1 g/L, simulations suggested increases in titer and specific productivity could be achieved for both photo-autotrophic and photomixotrophic conditions (Fig. 8b). Holding the
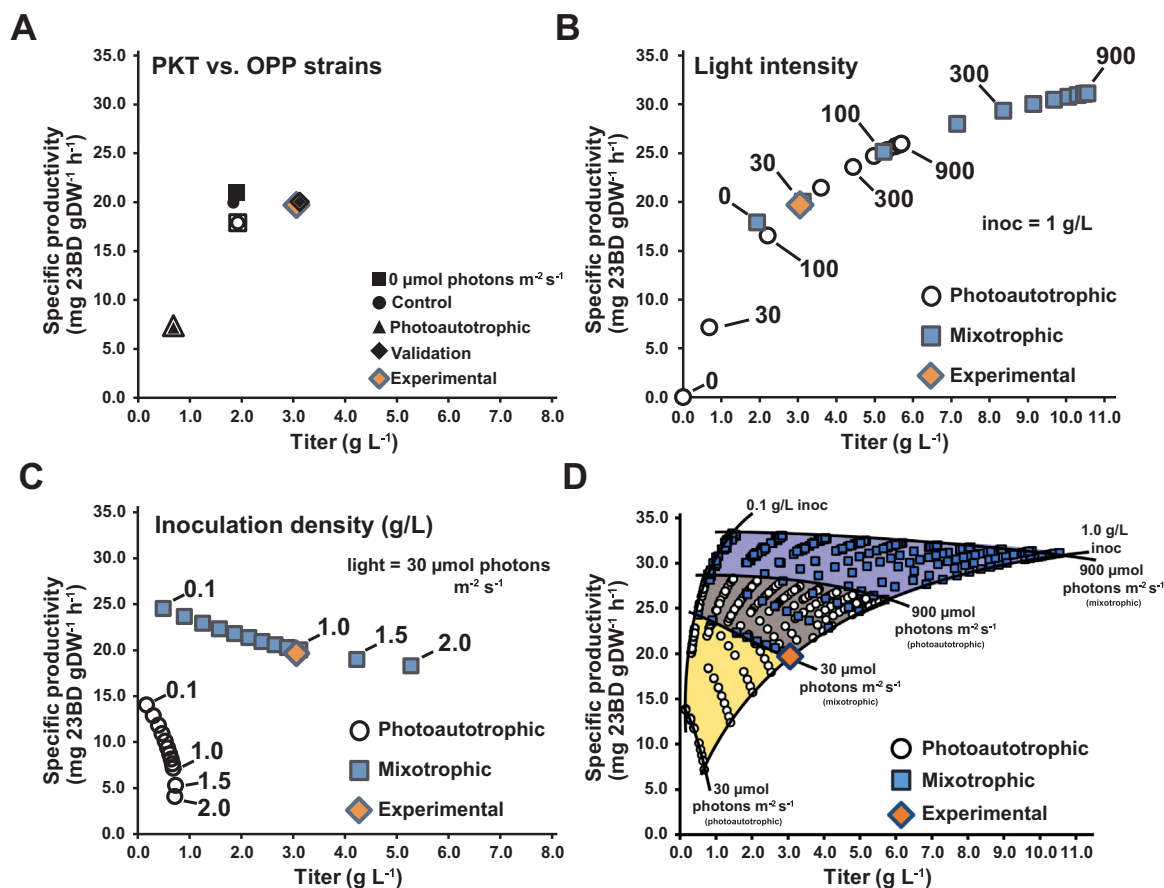
Fig. 7. Comparison of the phosphoketolase engineered pathway with oxidative pentose phosphate pathway. (A) Engineered pathway as described in Kanno et al. (2017) that routes extracellular glucose through the oxidative pentose phosphate toward 2,3-butanediol production. (B) Engineered pathway as described in this study that routes includes a phosphoketolase bypass toward 2,3-butanediol production. Metabolic reactions and metabolites are indicated by their BiGG identifier (bigg.ucsd.edu). Flux values are in units mmol gram^{-1} DW h^{-1}.

Fig. 8. Engineering photoautotrophic and photomixotrophic production of 2,3-butanediol in *S. elongatus*. (A) Specific productivity versus titer comparison of phosphoketolase (PKT) design (this study) with the oxidative pentose phosphate (OPP) engineered pathway as described in Kanno et al. (2017). Solid and open markers represent OPP and PKT values respectively. Control marker: no carbon fixation (Rubisco bounds = 0). Validation marker: *in silico* simulation of the experimental conditions reported in Kanno et al. (2017) (inoculation density: 1 g/L, light:30 μmol photon m^{-2} s^{-1}). (B) Specific productivity versus titer as a function of increasing light intensity. Select PAR values, in units of μmol photon m^{-2} s^{-1}, are indicated. (C) Specific productivity versus titer as a function of increasing inoculation density. (D) Specific productivity versus titer production envelope as a function of inoculation density and light intensity. Yellow shaded region: photoautotrophy. Blue shaded region: photomixotrophy. For all panels the experimental value as reported in Kanno et al. (2017) is shown and the total simulated culture duration was 3 days.

light intensity constant at 30 μmol photon m^{-2} s^{-1} and varying the inoculation density indicated the photoautotrophic condition was more sensitive to the cell density compared to the photomixotrophic condition (Fig. 8c). We assessed the full production envelope from an inoculation density of 0.1–1 g/L and irradiance values from 30 to 900 μmol photon m^{-2} s^{-1}. The simulations suggested dramatic improvements in both 23BD titer and specific productivity could be achieved by increasing the available light (Fig. 8d). Additionally, the impact to production yields caused by high inoculation densities was dramatically attenuated at high irradiances. While it is important to mention these results are based on the photoautotrophic P$_O$ vs. QF curves, even the photoautotrophic condition achieved theoretical titers 2-fold higher than the published photomixotrophic values with increased specific productivity.

4. Discussion

In this study we combined photophysiology constraints with a genome-scale model of *S. elongatus* PCC 7942 to predict metabolic differences between low and high light acclimated cultures. Overall, the model underestimated the growth rate at both high and low light but flux predictions were in good agreement with experimentally determined values. The genome-scale model predictions allowed for an assessment of excitation energy routing through the photosystem as a result of excess light absorption. Finally, we employed this modeling

construct to assess and improve current *S. elongatus* production strategies for 2,3-butanediol.

The photophysiology constraints resulted in accurate predictions of photoautotrophic growth. Whole cell absorption spectrum, cell dry weight and oxygen evolution are widely accessible experimental techniques that are often used to characterize photophysiology (Wagner et al., 2006). When coupled to genome-scale modeling, these inputs provided a detailed assessment of cellular metabolism to include growth rate and reaction fluxes. Such inputs could be used for real-time monitoring and/or process control parameters of large-scale, light-driven bioprocesses engineering.

While the upper bound of the simulations values approached the range of the experimental observations, the model tended to underestimate the growth rate at both high and low light. When determining the oxygen evolution rate, we did not supplement the sample with exogenous bicarbonate as it has been reported to affect photophysiology (Shimakawa et al., 2018). However, based on the cell densities used and photosynthetic rates observed, it is likely the samples became carbon limited during the oxygen evolution experiment. This likely would have reduced P$_{max}$ of the P$_O$ vs. QF curve used to parameterize the model resulting in a underestimation of the growth rate.

Parsimonious FBA reaction fluxes predicted by the genome-scale model were consistent with experimental ^{13}C metabolic flux analysis (Jazmin et al., 2017; Abernathy et al., 2017). The observed accuracy is partially due to the non-redundant nature of the *S. elongatus* metabolic

network. This lack of redundancy decreases the number of feasible flux states at the network level; evident by the similarity in experimental reaction fluxes in both ^{13}C MFA studies. The agreement between the model predictions and MFA data suggests the photophysiology parameters are dominant constraints on photoautotrophy and the FBA assumption of optimality is appropriate. These factors coupled with emerging methods for combining constraint-based modeling with quantitative -omics data (Yurkovich and Palsson, 2018) brings a wide variety of phenotypes of interest to the phototrophic community into scope for *in silico* modeling.

While there were discrepancies in the simulation flux predictions and experimental data, the experimental values fell within the flux range of equally optimal solutions. For the high light/fast growth rate comparison (Fig. 6), the primary differences were in the Calvin-Benson cycle phosphatase reactions. The experimental values for these reactions did fall within the flux ranges determined by flux variability analysis (FVA) (Fig. 5c). The wide flux ranges reported by FVA are due to the fact these phosphatases are coupled to ATP-consuming kinases. As the GAM/NGAM assessment indicated, there was an excess of ATP at both LL and HL. Thus, when FVA is maximizing flux through the phosphatase, the corresponding kinase reaction has a large pool of ATP to drive the reaction pair resulting in a wide flux range. Despite these discrepancies, the overall flux into and out of the Calvin-Benson cycle was accurately predicted by the model. For the low light/slow growth rate comparison (Fig. 4), the primary differences were around the hypothesized malate dehydrogenase reaction. This MDH bypass of pyruvate kinase is hypothesized to be necessary due to regulatory inhibition of pyruvate kinase (Knowles et al., 2001). The MDH reaction, which has yet to be ascribed to a gene in *S. elongatus*, was added to our GEM based on biochemical evidence from MFA (Jazmin et al., 2017). Regulatory mechanisms are not included in the genome-scale model; thus, the default prediction is for the bypass to not carry flux. While the pFBA solution predicted the MDH reaction carried no flux, the FVA flux ranges for this reaction were quite wide. Like the HL/fast growth rate comparison above, this was due to an ATP-coupled reaction (phosphoenolpyruvate synthase) driving flux through a loop that included MDH. Data-dependent incorporation of the PYK regulatory mechanism into a GEM could more accurately constrain the flux through this bypass. Of note, despite the biochemical evidence from MFA showing an MDH-mediated bypass of PYK, PYK is essential in vivo (Rubin et al., 2015). Therefore, in *S. elongatus*, the endogenous MDH-mediated PYK bypass cannot carry sufficient flux to maintain cell viability in the absence of PYK.

An advantage of genome-scale modeling over ^{13}C MFA is the ability to predict reaction fluxes beyond central metabolism. We used this capability to assess alternate energy flows in *S. elongatus*. Our simulations predicted approximately 37% and 58% of the absorbed photons at low and high light respectively, were in excess of growth requirements and energy transfer losses. These numbers are likely overestimates since the energy transfer losses included in the model are based on measurements in *S. elongatus* permeaplasts (Stamatakis et al., 2014) using chemical electron donor and acceptors; thus, they represent the most efficient energy transfer rates. Leveraging recent developments in cyanobacterial PAM fluorometry techniques (Ogawa et al., 2017) may help constrain the physiological values. Still, up to 40% of photosynthetic flux was reportedly directed to a reductant-mediated oxygen consuming AET reaction in the cyanobacterium *Synechocystis* (Helman, 2005). Additionally, our predicted PSI/PSII ratio of 3.2 is consistent with a measured ratio of 3.4 at similar light levels (Joshua and Mullineaux, 2005), suggesting our simulated values are in a biologically realistic range.

The model predicts an increase in excitation energy directed to PSI with an increase in QF (Table 4), consistent with known state transitions in cyanobacteria (Mullineaux, 2004). Additionally, our prediction of increased cyclic electron flow at high light, evident by increased flux through the NDH-1 complex, is in agreement with the known role of

this complex in cyanobacteria (Ohkawa et al., 2000; Bernat et al., 2010). The absolute fluxes through PSII versus PSI depends on accurate accounting of the metabolic cost of ROS detoxification at both reaction centers. Currently, the metabolic cost to repair the D1 protein, as represented in the model, drives the predicted excitation energy routing. Additionally, the GEM assigns a ROS generation rate that scales linearly with reaction flux. The kinetics of ROS generation are likely not linear in vivo and properly constraining the flux-dependent ROS generation rates stands as an area of improvement for the GEM. Still, the fold change in predicted PSI versus PSII flux predicted by the model was in close agreement in the change in Y(II) at the experimental QF (Table 4). This suggests coupling photon uptake constraints with the GEM assumption of optimality results in accurate qualitative assessments of excitation energy routing between low and high light.

It should be emphasized that FBA and MFA are complementary methods. As our FVA analysis showed, often GEM simulations result in multiple mathematically-equivalent flux states for a given set of constraints. MFA results restrict these alternate, equivalent optima to a narrower, biologically realistic subset. MFA results also validate or refute assumptions in the GEM. For example, in *S. elongatus* a phosphoketolase bypass of glycolysis is feasible based on the genome annotation (Broddrick et al., 2016). The GEM uses a hypothesized constraint that limits this bypass flux. The agreement between the model predictions and MFA data validates this constraint on phosphoketolase flux. GEMs also support and extend discovery and engineering in MFA experiments. Metabolic reconstructions define the core metabolism of the organism, assisting in the development of the isotopomer models needed for MFA. Additionally, ^{13}C MFA experiments in phototrophs are resource intensive. A validated GEM can explore phenotypes and engineering strategies *in silico* prior to committing resources on experimental validation of the predictions. Finally, genome-scale models extend MFA flux measurement outside of central metabolism either through direct constraints (Martín et al., 2015) or by analyzing the full flux distribution from a simulation that was validated against MFA central carbon flux, as we have done in this study.

The framework presented in this study provided insights into an existing 23BD production strain. Computational analysis of the published data (Kanno et al., 2017) established the glucose uptake rate of the photomixotrophic strain as well as constrained the fraction of carbon allocated to biomass. This analysis included the culture vessel geometry, total culture volume, light intensity, inoculation density and photophysiology; all parameters that can be optimized during bioprocess design. Characterization of the engineered strain enabled an assessment of the theoretical yield, suggesting that an increase in irradiance would result in higher production titers. While our assessment assumed photophysiology parameters from our study, replacing the P_O vs. QF curve with an experimentally derived curve from the photomixotrophic strain would enable a more accurate characterization of the production culture. The phosphoketolase design suggested by our flux simulations may provide additional *S. elongatus* bioengineering solutions. In particular, growth-coupled engineering strategies could be developed for bioproducts that are synthesized from the acetyl-CoA pool, such as isoprene (Gao et al., 2016) and acetone (Chwa et al., 2016). Additionally, this modeling framework can be coupled to models of dark metabolism to look at light-driven productivity during day/night cycles.

5. Conclusions

Engineering of cyanobacteria shows promise for generating energy-dense products with minimal input requirements. In this study we presented an *in silico* methodology for accurately characterizing photoautotrophic metabolism. These experimentally accessible constraints enable phototrophic genome-scale engineering equivalent to classical heterotrophic *in silico* design. Additionally, by incorporating photophysiology constraints with engineering design, we were able to assess

an existing photomixotrophic engineering strategy and revealed the current design was light limited. Coupling genome-scale modeling-driven *in silico* design with experimental validation, to include ^{13}C metabolic flux analysis, is a promising strategy to accelerate the iterative bioprocess design of light-driven metabolic engineering strategies.

Competing financial interests

The authors declare no competing financial interests.

Author Contribution

J.T.B.: Conceptualization, Formal analysis, Investigation, Writing - original draft; D.G.W.: Investigation, Writing - review & editing; D.J.: Investigation, Writing - review & editing; S.S.G.: Resources Writing - review & editing; G.P.: Conceptualization, Methodology , Resources, Supervision, Writing - review & editing; B.O.P.: Conceptualization, Methodology , Resources, Supervision, Writing - review & editing

Appendix A. Supplementary data

Supplementary data associated with this article can be found in the online version at doi:10.1016/j.ymben.2018.11.001.

References

Abernathy, M.H., Yu, J., Ma, F., Liberton, M., Ungerer, J., Hollinshead, W.D., Gopalakrishnan, S., He, L., Maranas, C.D., Pakrasi, H.B., Allen, D.K., Tang, Y.J., 2017. Deciphering cyanobacterial phenotypes for fast photoautotrophic growth via isotopically nonstationary metabolic flux analysis. Biotechnol. Biofuels 10 (1), 273. https://doi.org/10.1186/s13068-017-0958-y.⟨URL ⟨https://biotechnologyforbiofuels.biomedcentral.com/articles/10.1186/s13068-017-0958-y⟩⟩.

Adebiyi, A.O., Jazmin, L.J., Young, J.D., 2014. 13c flux analysis of cyanobacterial metabolism. Photosynth. Res. 126 (1), 19–32. https://doi.org/10.1007/s11120-014-0045-1.

Allakhverdiev, S.I., Murata, N., 2004. Environmental stress inhibits the synthesis de novo of proteins involved in the photodamage-repair cycle of Photosystem II in Synechocystis sp. PCC 6803. Biochim. Biophys. Acta 1657 (1), 23–32. https://doi.org/10.1016/j.bbabio.2004.03.003.⟨URL ⟨http://www.ncbi.nlm.nih.gov/pubmed/15238209⟩⟩.

Bennett, A., Bogorad, L., 1973. Complementary chromatic adaptation in a filamentous blue-green alga. J. Cell Biol. 58 (2), 419–435. https://doi.org/10.1083/jcb.58.2.419.

Bernat, G., Appel, J., Ogawa, T., Rogner, M., 2010. Distinct roles of multiple NDH-1 complexes in the cyanobacterial electron transport network as revealed by kinetic analysis of p700. reduction in various ndh-deficient mutants of synechocystis sp. strain PCC6803. J. Bacteriol. 193 (1), 292–295. https://doi.org/10.1128/jb.00984-10.

Broddrick, J.T., Rubin, B.E., Welkie, D.G., Du, N., Mih, N., Diamond, S., Lee, J.J., Golden, S.S., Palsson, B.O., 2016. Unique attributes of cyanobacterial metabolism revealed by improved genome-scale metabolic modeling and essential gene analysis. Proc. Natl. Acad. Sci. USA 113 (51), E8344–E8353. https://doi.org/10.1073/pnas.1613446113.⟨URL ⟨http://www.pnas.org/content/113/51/E8344.abstract⟩⟨http://www.pnas.org/lookup/doi/10.1073/pnas.1613446113⟩⟩.

Carroll, A.L., Case, A.E., Zhang, A., Atsumi, S., 2018. Metabolic engineering tools in model cyanobacteria. Metab. Eng. https://doi.org/10.1016/j.ymben.2018.03.014.

Chwa, J.-W., Kim, W.J., Sim, S.J., Um, Y., Woo, H.M., 2016. Engineering of a modular and synthetic phosphoketolase pathway for photosynthetic production of acetone from CO2inSynechococcus elongatusPCC 7942 under light and aerobic condition. Plant

Biotechnol. J. 14 (8), 1768–1776. https://doi.org/10.1111/pbi.12536.

Ebrahim, A., Lerman, J.A., Palsson, B.O., Hyduke, D.R., 2013. COBRApy: constraints-based Reconstruction and analysis for python. BMC Syst. Biol. 7 (1), 74. https://doi.org/10.1186/1752-0509-7-74.⟨URL ⟨http://www.ncbi.nlm.nih.gov/pubmed/23927696⟩⟨http://bmcsystbiol.biomedcentral.com/articles/10.1186/1752-0509-7-74⟩⟨http://www.pubmedcentral.nih.gov/articlerender.fcgi?artid=PMC3751080⟩⟩.

Feist, A.M., Palsson, B.O., 2010. The biomass objective function. Curr. Opin. Microbiol. 13 (3), 344–349. https://doi.org/10.1016/j.mib.2010.03.003.(URL ⟨http://www.ncbi.nlm.nih.gov/pubmed/20430689⟩⟨http://linkinghub.elsevier.com/retrieve/pii/S1369527410000512⟩).

Gao, X., Gao, F., Liu, D., Zhang, H., Nie, X., Yang, C., 2016. Engineering the methylerythritol phosphate pathway in cyanobacteria for photosynthetic isoprene production from CO2. Energy Environ. Sci. 9 (4), 1400–1411. https://doi.org/10.1039/c5ee03102h.

Gudmundsson, S., Agudo, L., Nogales, J., 2017. Applications of genome-scale metabolic models of microalgae and cyanobacteria in biotechnology. In: Schulze, E.D., Caldwell, M.M. (Eds.), Microalgae-Based Biofuels and Bioproducts. Elsevier, Berlin, Heidelberg, pp. 93–111. https://doi.org/10.1016/b978-0-08-101023-5.00004-2.

Helman, Y., 2005. Fractionation of the three stable oxygen isotopes by oxygen-producing and oxygen-consuming reactions in photosynthetic organisms. Plant Physiol. 138 (4), 2292–2298. https://doi.org/10.1104/pp.105.063768.

Hirokawa, Y., Maki, Y., Tatsuke, T., Hanai, T., 2016. Cyanobacterial production of 1,3-propanediol directly from carbon dioxide using a synthetic metabolic pathway. Metab. Eng. 34, 97–103. https://doi.org/10.1016/j.ymben.2015.12.008.

Jallet, D., Caballero, M.A., Gallina, A.A., Youngblood, M., Peers, G., 2016. Photosynthetic physiology and biomass partitioning in the model diatom phaeodactylum tricornutum grown in a sinusoidal light regime. Algal Res. 18, 51–60. https://doi.org/10.1016/j.algal.2016.05.014.(URL ⟨http://www.sciencedirect.com/science/article/pii/S2211926416301709⟩⟨https://www.sciencedirect.com/science/article/pii/S2211926416301709⟩).

Jazmin, L.J., Xu, Y., Cheah, Y.E., Adebiyi, A.O., Johnson, C.H., Young, J.D., 2017. Isotopically nonstationary 13C flux analysis of cyanobacterial isobutyraldehyde production. Metab. Eng. 42, 9–18. https://doi.org/10.1016/j.ymben.2017.05.001.(URL ⟨http://www.ncbi.nlm.nih.gov/pubmed/28479191⟩⟨http://www.pubmedcentral.nih.gov/articlerender.fcgi?artid=PMC5660605⟩).

Joshua, S., Mullineaux, C.W., 2005. The rpaC gene product regulates phycobilisome-photosystem II interaction in cyanobacteria. Biochim. Biophys. Acta (BBA) - Bioenergy 1709 (1), 58–68. https://doi.org/10.1016/j.bbabio.2005.06.005.

Kanno, M., Atsumi, S., 2016. Engineering an obligate photoautotrophic cyanobacterium to utilize glycerol for growth and chemical production. ACS Synth. Biol. 6 (1), 69–75. https://doi.org/10.1021/acssynbio.6b00239.

Kanno, M., Carroll, A.L., Atsumi, S., 2017. Global metabolic rewiring for improved CO2 fixation and chemical production in cyanobacteria. Nat. Commun. 8, 14724. https://doi.org/10.1038/ncomms14724.(URL ⟨https://doi.org/10.1038%2Fncomms14724⟩).

Kim, W.J., Kim, H.U., Lee, S.Y., 2017. Current state and applications of microbial genome-scale metabolic models. Curr. Opin. Syst. Biol. 2, 10–18. https://doi.org/10.1016/j.coisb.2017.03.001.(URL ⟨https://doi.org/10.1016%2Fj.coisb.2017.03.001⟩).

King, Z.A., Dräger, A., Ebrahim, A., Sonnenschein, N., Lewis, N.E., Palsson, B.O., 2015a. Escher A web application for building, sharing, and embedding data-rich visualizations of biological pathways. PLoS Comput. Biol. 11 (8), e1004321. https://doi.org/10.1371/journal.pcbi.1004321.(URL ⟨http://dx.plos.org/10.1371/journal.pcbi.1004321⟩⟨http://www.ncbi.nlm.nih.gov/pubmed/26313928⟩⟨http://www.pubmedcentral.nih.gov/articlerender.fcgi?artid=PMC4552468⟩).

King, Z.A., Lloyd, C.J., Feist, A.M., Palsson, B.O., 2015b. Next-generation genome-scale models for metabolic engineering. Curr. Opin. Biotechnol. 35, 23–29. https://doi.org/10.1016/j.copbio.2014.12.016.

Kirilovsky, D., Kerfeld, C.A., 2012. The orange carotenoid protein in photoprotection of photosystem ii in cyanobacteria. Biochim. Biophys. Acta (BBA) - Bioenergy 1817 (1), 158–166. https://doi.org/10.1016/j.bbabio.2011.04.013.(photosystem II. URL ⟨http://www.sciencedirect.com/science/article/pii/S0005272811000983⟩).

Knoop, H., Grndel, M., Zilliges, Y., Lehmann, R., Hoffmann, S., Lockau, W., Steuer, R., 2013. Flux balance analysis of cyanobacterial metabolism: the metabolic network of synechocystis sp. PCC 6803. PLoS Comput. Biol. 9 (6), e1003081. https://doi.org/10.1371/journal.pcbi.1003081.

Knowles, V.L., Smith, C.S., Smith, C.R., Plaxton, W.C., 2001. Structural and regulatory properties of pyruvate kinase from the cyanobacterium synechococcusPCC 6301. J. Biol. Chem. 276 (24), 20966–20972. https://doi.org/10.1074/jbc.m008878200.

Kramer, D.M., Johnson, G., Kiirats, O., Edwards, G.E., 2004. New fluorescence parameters for the determination of QARedox state and excitation energy fluxes. Photosynth. Res. 79 (2), 209–218. https://doi.org/10.1023/b:pres.0000015391.99477.0d.

Lan, E.I., Wei, C.T., 2016. Metabolic engineering of cyanobacteria for the photosynthetic production of succinate. Metab. Eng. 38, 483–493. https://doi.org/10.1016/j.ymben.2016.10.014.

Lan, E.I., Chuang, D.S., Shen, C.R., Lee, A.M., Ro, S.Y., Liao, J.C., 2015. Metabolic engineering of cyanobacteria for photosynthetic 3-hydroxypropionic acid production from CO 2 using synechococcus elongatus PCC 7942. Metab. Eng. 31, 163–170. https://doi.org/10.1016/j.ymben.2015.08.002.

Lea-Smith, D.J., Bombelli, P., Vasudevan, R., Howe, C.J., 2016. Photosynthetic, respiratory and extracellular electron transport pathways in cyanobacteria. Biochim. Biophys. Acta (BBA) - Bioenergy 1857 (3), 247–255. https://doi.org/10.1016/j.bbabio.2015.10.007.

Levering, J., Broddrick, J., Zengler, K., 2015. Engineering of oleaginous organisms for lipid production. Curr. Opin. Biotechnol. 36, 32–39. https://doi.org/10.1016/j.copbio.2015.08.001.(URL ⟨https://linkinghub.elsevier.com/retrieve/pii/S0958166915001007⟩⟨http://www.ncbi.nlm.nih.gov/pubmed/26319892⟩⟨http://

www.sciencedirect.com/science/article/pii/S0958166915001007〉).

Lewis, N.E., Hixson, K.K., Conrad, T.M., Lerman, J.A., Charusanti, P., Polpitiya, A.D., Adkins, J.N., Schramm, G., Purvine, S.O., Lopez-Ferrer, D., Weitz, K.K., Eils, R., König, R., Smith, R.D., Palsson, B.Ø., 2010. Omic data from evolved E. coli are consistent with computed optimal growth from genome-scale models. Mol. Syst. Biol. 6, 390. https://doi.org/10.1038/msb.2010.47.(URL 〈http://msb.embopress.org/cgi/doi/10.1038/msb.2010.47〉〈http://www.ncbi.nlm.nih.gov/pubmed/20664636〉).

Machado, D., Herrgård, M., 2014. Systematic evaluation of methods for integration of transcriptomic data into constraint-based models of metabolism. PLoS Comput. Biol. 10 (4), e1003580. https://doi.org/10.1371/journal.pcbi.1003580.

Martín, H.G., Kumar, V.S., Weaver, D., Ghosh, A., Chubukov, V., Mukhopadhyay, A., Arkin, A., Keasling, J.D., 2015. A method to constrain genome-scale models with 13c labeling data. PLoS Comput. Biol. 11 (9), e1004363. https://doi.org/10.1371/journal.pcbi.1004363.

McEwen, J.T., Machado, I.M.P., Connor, M.R., Atsumi, S., 2012. Engineering Synechococcus elongatus PCC 7942 for continuous growth under diurnal conditions. Appl. Environ. Microbiol. 79 (5), 1668–1675. https://doi.org/10.1128/aem.03326-12.

Moore, L.R., Goericke, R., Chisholm, S.W., 1995. Comparative physiology of synechococcus and prochlorococcus: influence of light and temperature on growth, pigments, fluorescence and absorptive properties. Mar. Ecol. Prog. Ser. 116 (1), 259–275(URL 〈https://www.jstor.org/stable/44635011〉).

Mullineaux, C.W., 2004. State transitions: an example of acclimation to low-light stress. J. Exp. Bot. 56 (411), 389–393. https://doi.org/10.1093/jxb/eri064.

Nogales, J., Gudmundsson, S., Knight, E.M., Palsson, B.O., Thiele, I., 2012. Detailing the optimality of photosynthesis in cyanobacteria through systems biology analysis. Proc. Natl. Acad. Sci. USA 109 (7), 2678–2683. https://doi.org/10.1073/pnas.1117907109.(URL 〈http://www.ncbi.nlm.nih.gov/pubmed/22308420〉〈http://www.pubmedcentral.nih.gov/articlerender.fcgi?artid=PMC3289291〉〈http://www.pnas.org/cgi/doi/10.1073/pnas.1117907109〉).

Ogawa, T., Misumi, M., Sonoike, K., 2017. Estimation of photosynthesis in cyanobacteria by pulse-amplitude modulation chlorophyll fluorescence: problems and solutions. Photosynth. Res. 133 (1), 63–73. https://doi.org/10.1007/s11120-017-0367-x.

Ohkawa, H., Pakrasi, H.B., Ogawa, T., 2000. Two types of functionally distinct NAD(p)h dehydrogenases inSynechocystissp. strain PCC6803. J. Biol. Chem. 275 (41), 31630–31634. https://doi.org/10.1074/jbc.m003706200.

Oliver, J.W.K., Machado, I.M.P., Yoneda, H., Atsumi, S., 2013. Cyanobacterial conversion of carbon dioxide to 2,3-butanediol. Proc. Natl. Acad. Sci. USA 110 (4), 1249–1254. https://doi.org/10.1073/pnas.1213024110.(URL 〈http://www.ncbi.nlm.nih.gov/pubmed/23297225〉〈http://www.pnas.org/lookup/doi/10.1073/pnas.1213024110〉).

Oliver, N.J., Rabinovitch-Deere, C.A., Carroll, A.L., Nozzi, N.E., Case, A.E., Atsumi, S., 2016. Cyanobacterial metabolic engineering for biofuel and chemical production. Curr. Opin. Chem. Biol. 35, 43–50. https://doi.org/10.1016/j.cbpa.2016.08.023.

Orth, J.D., Thiele, I., Palsson, B.O.Ø., 2010. What is flux balance analysis? Nat. Biotechnol. 28 (3), 245–248. https://doi.org/10.1038/nbt.1614.(URL 〈http://www.nature.com/articles/nbt.1614〉〈http://www.ncbi.nlm.nih.gov/pubmed/20212490〉).

Pérez, F., Granger, B.E., rez Fernando, P., 2007. IPython: a system for interactive scientific computing. Comput. Sci. Eng. 9 (3), 21–29. https://doi.org/10.1109/MCSE.2007.53.(URL 〈http://doi.ieeecomputersociety.org/10.1109/MCSE.2007.53〉〈http://ipython.org〉).

Platt, T., Gallegos, C.L., Harrison, W.G., 1980. Photoinhibition of photosynthesis in natural assemblages of marine-phytoplankton. J. Mar. Res. 38 (4), 687–701.

Ritchie, R.J., 2008. Universal chlorophyll equations for estimating chlorophylls a, b, c, and d and total chlorophylls in natural assemblages of photosynthetic organisms using acetone, methanol, or ethanol solvents. Photosynthetica 46 (1), 115–126. https://doi.org/10.1007/s11099-008-0019-7.

Rubin, B.E., Wetmore, K.M., Price, M.N., Diamond, S., Shultzaberger, R.K., Lowe, L.C., Curtin, G., Arkin, A.P., Deutschbauer, A., Golden, S.S., 2015. The essential gene set of a photosynthetic organism. Proc. Natl. Acad. Sci. USA 112 (48), E6634–43. https://doi.org/10.1073/pnas.1519220112.(URL 〈http://www.pnas.org/lookup/doi/10.1073/pnas.1519220112〉〈http://www.ncbi.nlm.nih.gov/pubmed/26508635〉〈http://www.pubmedcentral.nih.gov/articlerender.fcgi?artid=PMC4672817〉).

Schindelin, J., Rueden, C.T., Hiner, M.C., Eliceiri, K.W., 2015. The ImageJ ecosystem: an open platform for biomedical image analysis. Mol. Reprod. Dev. 82 (7–8), 518–529. https://doi.org/10.1002/mrd.22489.(URL 〈http://www.ncbi.nlm.nih.gov/pubmed/26153368〉〈http://doi.wiley.com/10.1002/mrd.22489〉〈http://www.pubmedcentral.nih.gov/articlerender.fcgi?artid=PMC5428984〉).

Schreiber, U., Bilger, W., Neubauer, C., 1995. Chlorophyll fluorescence as a nonintrusive indicator for rapid assessment of in vivo photosynthesis. In: Schulze, E.D., Caldwell, M.M. (Eds.), Ecophysiology of Photosynthesis. Springer, Berlin, Heidelberg, pp. 49–70. https://doi.org/10.1007/978-3-642-79354-7_3.

Schuurmans, R.M., van Alphen, P., Schuurmans, J.M., Matthijs, H.C.P., Hellingwerf, K.J., 2015. Comparison of the photosynthetic yield of cyanobacteria and green algae: different methods give different answers. PLoS One 10 (9), e0139061. https://doi.org/10.1371/journal.pone.0139061.

Shimakawa, G., Shaku, K., Miyake, C., 2018. Reduction-induced suppression of electron flow (rise) is relieved by non-atp-consuming electron flow in synechococcus elongatus pcc 7942. Front. Microbiol. 9, 886. https://doi.org/10.3389/fmicb.2018.00886.(URL 〈https://www.frontiersin.org/article/10.3389/fmicb.2018.00886〉).

Stamatakis, K., Tsimilli-Michael, M., Papageorgiou, G.C., 2014. On the question of the light-harvesting role of β-carotene in photosystem II and photosystem I core complexes. Plant Physiol. Biochem. PPB 81, 121–127. https://doi.org/10.1016/j.plaphy.2014.01.014.(URL 〈http://linkinghub.elsevier.com/retrieve/pii/S098194281400028X〉〈http://www.ncbi.nlm.nih.gov/pubmed/24529497〉).

Tichy, M., Vermaas, W., Information, U., Pcc, S., Tichy, M., Vermaas, W., 1999. In vivo role of catalase-peroxidase in synechocystis sp. strain pcc 6803. J. Bacteriol. 1875–1882.

Wagner, H., Jakob, T., Wilhelm, C., 2006. Balancing the energy flow from captured light to biomass under fluctuating light conditions. New Phytol. 169 (1), 95–108. https://doi.org/10.1111/j.1469-8137.2005.01550.x.(URL 〈http://www.ncbi.nlm.nih.gov/pubmed/16390422〉〈http://doi.wiley.com/10.1111/j.1469-8137.2005.01550.x〉).

Young, J.D., Shastri, A.A., Stephanopoulos, G., Morgan, J.A., 2011. Mapping photoautotrophic metabolism with isotopically nonstationary 13c flux analysis. Metab. Eng. 13 (6), 656–665. https://doi.org/10.1016/j.ymben.2011.08.002.

Yurkovich, J.T., Palsson, B.O., 2018. Quantitative -omic data empowers bottom-up systems biology. Curr. Opin. Biotechnol. 51, 130–136. https://doi.org/10.1016/j.copbio.2018.01.009.(systems biology ○ Nanobiotechnology. URL 〈http://www.sciencedirect.com/science/article/pii/S0958166917302276〉).

1 **Supplementary Material for "Predicting the metabolic capabilities of *S. elongatus* PCC 7942 adapted to different**
2 **light regimes"**

3 Authors: Jared T. Broddrick, David G. Welkie, Denis Jallet, Susan S. Golden, Graham Peers and Bernhard O. Palsson
4 The following Supporting Information is available for this article:
5 **Modeling files can be found at http://systemsbiology.ucsd.edu/Downloads/SupplementalData**
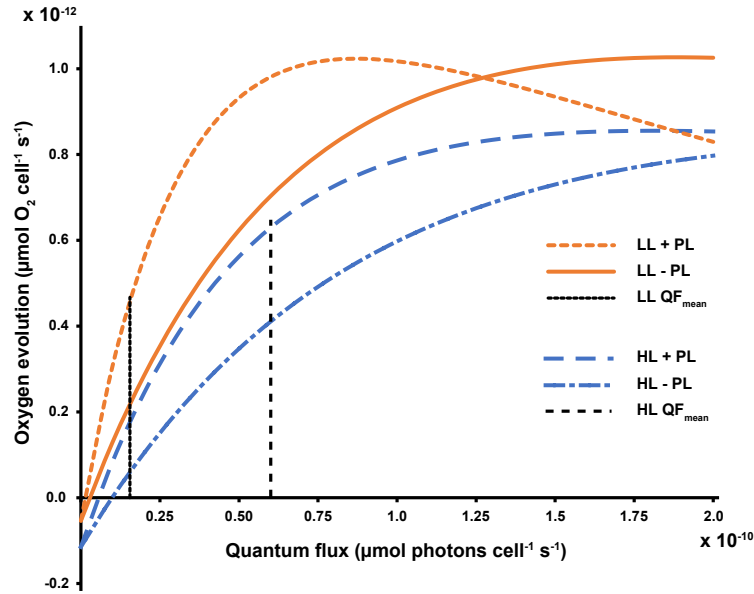

Fig. S1. Effect of path length correction on quantum flux calculations *S. elongatus*. Accounting for cell shading in the determination of quantum flux affects the calculated oxygen evolution rate at the experimental conditions. +/- PL refers to plots with (+) or without (-) accounting for path length. Abbreviations. LL: low light, HL: high light, PL: path length, QF: quantum flux.
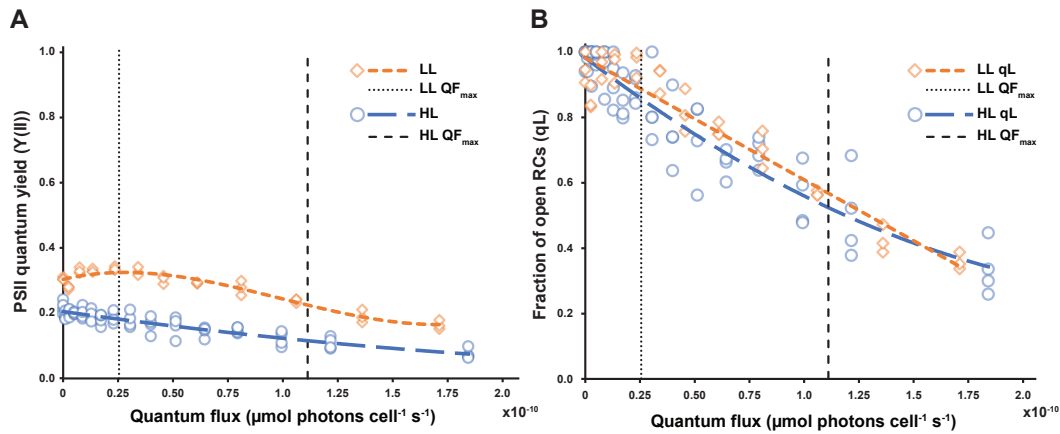

Fig. S2. Chlorophyll fluorescence parameters versus quantum flux for *S. elongatus*. (A) Quantum yield of photosystem II (PSII) versus QF curves. The maximal quantum yield (Fv/Fm) is equal to the y-intercept of the curves. (B) Fraction of open reaction centers (RCs) versus quantum flux. Vertical dashed lines represent the maximum quantum flux received by the cultures at the experimental irradiance. Abbreviations. LL: low light, HL: high light, QF: quantum flux.
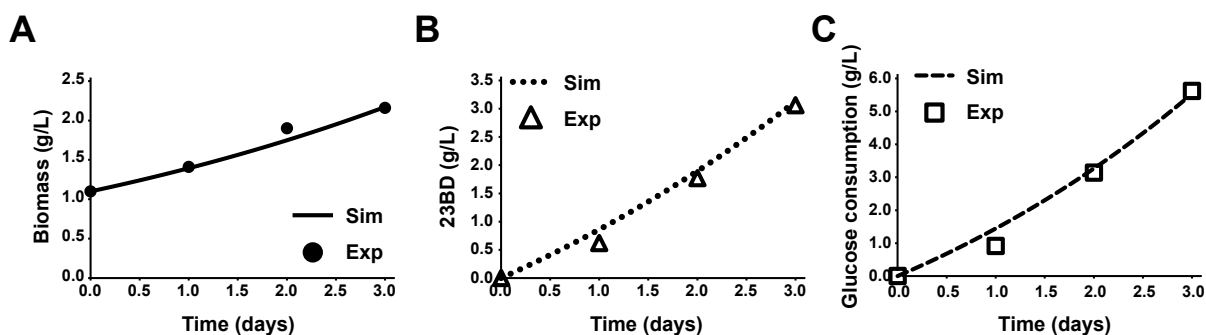
Fig. S3. In silico recapitulation of an *S. elongatus* strain designed for 2,3-butanediol production. (A) Biomass, (B) 2,3-butanediol (23BD) production and (C) glucose consumption over the first 3 days of culturing. Experimental data points (Exp) were taken from published values (1). Simulations were set with the biomass production at 20% of the maximum and a glucose uptake rate of 0.27 mmol glc gDW^{-1} h^{-1}

.

Table S1. Content edits to *i*JB785 in the construction of *i*JB792.

Reaction ID	Reaction name	Notes
MPTSS	Molybdopterin synthase sulfurylase	Added. Molybdopterin cofactor biosynthesis.
MOADSUx	MoaD sulfuration (nadh, assumed)	Added. Molybdopterin cofactor biosynthesis.
GTPC	GTP 3,8-cyclase	Added. Molybdopterin cofactor biosynthesis.
CPMPS	Cyclic pyranopterin monophosphate synthase	Added. Molybdopterin cofactor biosynthesis.
MPTS	Molybdopterin synthase	Added. Molybdopterin cofactor biosynthesis.
MPTAT	Molybdopterin adenylyltransferase	Added. Molybdopterin cofactor biosynthesis.
MOCOS	Molybdenum cofactor synthase	Added. Molybdopterin cofactor biosynthesis.
MDH	Malate dehydrogenase	Added. Based on fluxomics data (2). Gene reaction rule unknown.
ORNTA	Ornithine transaminase	Deleted. Gene model results in a truncated protein that appears to be inactive *in vivo* (3)

6   1. Kanno M, Carroll AL, Atsumi S (2017) Global metabolic rewiring for improved CO2 fixation and chemical production in cyanobacteria. *Nature Communications* 8:14724.
7   2. Jazmin LJ, et al. (2017) Isotopically nonstationary 13C flux analysis of cyanobacterial isobutyraldehyde production. *Metabolic engineering* 42:9–18.
8   3. Broddrick JT, et al. (2016) Unique attributes of cyanobacterial metabolism revealed by improved genome-scale metabolic modeling and essential gene analysis. *Proceedings of the National Academy*
9   *of Sciences* 113(51):E8344–E8353.